University of Nevada, Reno

Probing exotic fields with networks of atomic clocks

A thesis submitted in partial fulfillment of the requirements
for the degree of Master of Science in Physics

by

Conner Dailey

Dr. Andrei Derevianko, Thesis Advisor

August, 2019

University of Nevada, Reno,

The Graduate School

We recommend that the thesis

prepared under our supervision by

CONNER BURKE DAILEY

entitled

Probing exotic fields with networks of atomic clocks

be accepted in partial fulfillment of the

requirements for the degree of

MASTER OF SCIENCE

Andrei Derevianko, Ph.D., Advisor

Geoffrey Blewitt, Ph.D., Committee Member

A. Grant Schissler, Ph.D., Graduate School Representative

David W. Zeh, Ph.D., Dean, Graduate School

August, 2019

UNIVERSITY OF NEVADA, RENO

Abstract

GPS.DM Observatory

Physics Department

Master of Science

Probing exotic fields with networks of atomic clocks

by Conner Dailey

An exotic light field (ELF) is a class of field beyond the standard model that could be produced in high-energy astrophysical events with enough amplitude to be detected with precision measurement sensors. A model that describes an ELF as a pulse of ultra-relativistic matter waves and an estimate of the sensitivity for current and future networks of atomic clocks to detect ELFs is developed here. The global positioning system (GPS) is presented as an existing network of atomic clocks that has the potential to probe ELFs. A first proof-of-principle search for ELFs emitted as bursts from the GW170817 neutron star merger was performed with data from GPS. Although no concrete evidence was found for ELFs, a foundation has been produced for future searches for ELFs originating from many other astrophysical events, such as gamma ray bursts, black hole mergers, and solar flares for the last $\sim$20 years of GPS operation.

Acknowledgements

I give great thanks to my advisors who have given me guidance from my undergraduate years until now. Much of this work has been guided and edited by those involved in both the GPS.DM and GNOME collaborations, especially Dr. Andrei Derevianko, Dr. Derek Jackson Kimball, and Dr. Geoffrey Blewitt. I am also grateful to JPL for their collaboration in generating data.

This work was supported in part by the National Science Foundation.

Contents

List of Tables

List of Figures

List of Abbreviations

CDDIS	**C**rustal **D**ynamics **D**ata **I**nformation **S**ystem
DM	**D**ark **M**atter
DFT	**D**iscrete **F**ourier **T**ransform
ECEF	**E**arth **C**entered **E**arth **F**ixed (Reference Frame)
ECI	**E**arth **C**entered **I**nertial (Reference Frame)
ELF	**E**xotic **L**ight **F**ield
GNOME	**G**lobal **N**etwork of **O**ptical **M**agnetometers for **E**xotic Physics
GPS	**G**lobal **P**ositioning **S**ystem
GNSS	**G**lobal **N**avigation **S**atellite **S**ystem
ICRF	**I**nternational **C**elestial **R**eference **F**rame
IERS	**I**nternational **E**arth **R**otation and Reference Frame **S**ervice
JPL	**J**et **P**ropulsion **L**aboratory
LIGO	**L**aser **I**nterferometer **G**ravitational-Wave **O**bservatory
NASA	**N**ational **A**eronautics and **S**pace **A**dministration
NGC	**N**ew **G**eneral **C**atalog
NSM	**N**eutron **S**tar **M**erger
RINEX	**R**eceiver **In**dependent **Ex**change Format
RMS	**R**oot **M**ean **S**quare
UTC	(**C**oordinated) **U**niversal **T**ime

Physical Constants

Speed of Light	$c = 2.997\,924\,58 \times 10^{8}\,\mathrm{m\,s^{-1}}$ (exact)
Planck Energy	$E_P = 1.956\,081 \times 10^{8}\,\mathrm{J}$
Elementary Charge	$e = 1.602\,176\,634 \times 10^{-19}$ C (exact)
Newton's Gravitational Constant	$G = 6.674\,30 \times 10^{-11}\ \mathrm{m^3kg^{-1}s^{-2}}$
Reduced Planck's Constant	$\hbar = 1.054\,571\,817 \times 10^{-34}\ \mathrm{J\,s}$ (exact)
Solar Mass	$M_\odot = 1.9884 \times 10^{30}\,\mathrm{kg}$
Electron Mass	$m_e = 9.109\,383\,701\,5 \times 10^{-31}$ kg
Proton Mass	$m_p = 1.672\,621\,923\,69 \times 10^{-27}$ kg
Fine Structure Constant	$\alpha = 7.297\,352\,569\,3 \times 10^{-3}$

List of Symbols

Symbol	Description	SI Unit
A	ELF amplitude	$\sqrt{\mathrm{J\,m}}$
A_0	initial ELF amplitude	$\sqrt{\mathrm{J\,m}}$
$A(k)$	ELF Fourier amplitudes	$\sqrt{\mathrm{J\,m}}$
$\tilde{C}$	one-sided power spectrum	-
$d_{a,j}$	data element	-
d_e	electromagnetic gauge modulus	-
ΔE	total ELF energy	J
L_0	ELF pulse initial width	m
m	mass	kg
N	number of DFT points	-
N_w	number of time windows	-
N_d	number of devices	-
$n_{a,j}$	noise element	-
k	wavevector magnitude	$\mathrm{m^{-1}}$
k_0	initial wavevector magnitude	$\mathrm{m^{-1}}$
R	distance from ELF source to Earth	m
r	radial coordinate	m
$s_{a,j}$	signal element	-
T	sampling interval	s
t	time coordinate	s
δt	ELF delay time	s
v_g	central ELF pulse group velocity	$\mathrm{m\,s^{-1}}$
Δv_g	ELF pulse group velocity spread	$\mathrm{m\,s^{-1}}$
γ	Lorentz factor	-
γ_X	linear coupling constant	/J
ε	excess power	-
κ_X	sensitivity coefficients	-
Λ_X	quadratic effective energy scale	J
ν	associated clock frequency	$\mathrm{s^{-1}}$
ρ	energy density	$\mathrm{J\,m^{-3}}$

σ_y	clock Allan deviation	-
τ	ELF signal duration at Earth	s
τ_0	initial ELF signal duration	s
ϕ	ELF field	$\sqrt{\mathrm{J\,m^{-1}}}$
ω	ELF angular frequency	$\mathrm{s^{-1}}$
ω_0	initial ELF angular frequency	$\mathrm{s^{-1}}$
$\Delta\omega$	ELF pulse angular frequency spread	$\mathrm{s^{-1}}$

Chapter 1

Introduction

1.1 A Brief History of GPS

In this section I will give a short history of the GPS constellation and a concise explanation on how it was designed and currently works. This information and further reading can be found in [1], [2], and [3]. GPS has 3 major parts, the control, space, and user segments. I will focus mainly on the control and space segments as they are of main relevance to this work.

The US Department of Defense designed and implemented GPS starting in 1978 with the launch of the first Block I satellite called NAVSTAR 1. A total of 11 of these prototype satellites were launched by 1985, to test the software and hardware of the system. Then 9 Block II satellites were launched by 1990, and by 1994, a full constellation of 24 satellites was completed with the introduction of Block IIA satellites. With this network size, it was then possible for users

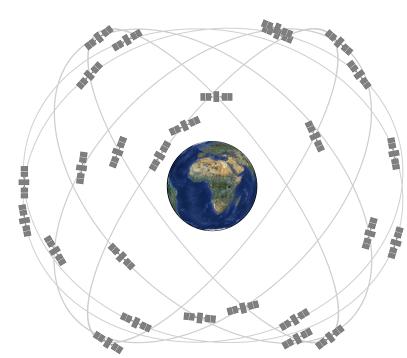

FIGURE 1.1: Artist's rendition of the expanded 24 slot GPS constellation, with 6 orbital planes [4].

of GPS to communicate with a minimum of 5 satellites at once, at any time or place on Earth. Full operational capacity of the network was declared in 1995. By 2008, a total of 57 GPS satellites had been successfully launched, many either being retired or acting as active spares in case of a satellite failure. At the time of this work, there are a few more iterations of satellites, including blocks IIR, IIR-M, and IIF, with Block III currently under development. The modern GPS satellite blocks are outlined in Table 1.1. The quality of the GPS raw data was dramatically improved when the artificial degradation of the GPS signal was removed on May 1, 2000. By the end of 2019, there will be about 20 years worth of high-quality GPS network time-series atomic clock data archived by JPL and available to the public. The quality of the GPS network improves with each modern satellite added to the network.

1.2 Inner Workings of GPS

This section outlines the operation of GPS in enough detail to be understood in the following chapters. GPS works by broadcasting microwave signals from satellites in medium-Earth orbit. The signals broadcast to the Earth by each satellite are driven by an atomic clock (either based on Rb or Cs energy transitions) on board.

1.2.1 The Space Segment

The original design of GPS had 24 satellite orbit slots using only 6 different orbital planes, which are labeled A-F. The orbits of the satellites are described in terms of the Keplerian elements, the relevant ones of which are defined by Fig. 1.2. Most of these elements are set by the design of the space segment.

Legacy Satellites		Modernized Satellites		
Block IIA	Block IIR	Block IIR-M	Block IIF	Block III
• L1 frequency broadcast for civil users • L1 and L2 frequencies broadcast for military users • 7.5-year design lifespan • Launched between 1990-1997	• On-board clock monitoring • Launched between 1990-1997	• All legacy signals • 2nd civilian signal on L2 frequency • New military "M code" signals • 7.5-year design lifespan • Launched between 2005-2009	• All Block IIR-M signals • 3rd civil signal on L5 frequency • Improved accuracy, signal strength, and quality • 12-year design lifespan • Launched between 2010-2016	• All Block IIF signals • 4th civil signal on L1 frequency • Enhanced signal reliability, accuracy, and integrity • 15-year design lifespan • Laser reflectors; search and rescue payloads • First launch in 2018
Clocks Onboard				
2 Rb and 2 Cs clocks	3 Rb clocks	3 Rb clocks	2 Rb clocks and 1 Cs clock	3 Rb clocks

Table 1.1: The modern GPS space segment, outlining the differences between satellite iterations. The GPS frequency band L1 operates at 1575.42 MHz, L2 at 1227.6 MHz, and L5 at 1176.45 MHz. This table is adapted from [4].

The orbits are approximately circular, with an inclination of 55° and a semi-major axis of 26559.7 km. The orbital planes are equally spaced about the equator, meaning each is separated by a difference in their longitude of the ascending nodes (also commonly refered to as the right ascension of the ascending node) of 60°. Within each orbital plane, the satellites are asymmetrically spaced by their true anomaly (or if measured from the ascending node can be described by the argument of latitude) by design. In 2011, the 24 slot network was expanded to contain 27 satellites for better visibility and accuracy. The positions for the 24 slot and the expanded 24 slot networks are outlined in Figure 1.3. The positions of the excess satellites in the network are typically placed near active satellites that are expected to require replacement the soonest. Although several satellites act as active spares, they still transmit data, so the effective atomic clock network size includes all non-retired satellites. In August 2017, the time period relevant to the analysis in the following chapters, there were 31 operational satellites in the GPS constellation.

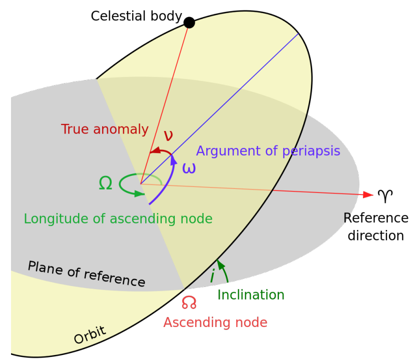

FIGURE 1.2: Definition of the orientation specifying Keplerian elements. The reference direction in this case is the x-axis of the ECI frame and the plane of reference is the Earth's equatorial plane. [4].

1.2.2 The Control Segment

The GPS space segement broadcasts microwave signals to the terrestrial control segment. This is mainly a network of specialized Earth-based GPS receivers referred to here as stations. Each station of Fig. 1.4 has a 4-character identifier and constantly measures the carrier phase of the microwaves signals from each satellite its view. This network includes the US Naval Observatory (USNO) master clock station USN3 in Washington D.C., with a

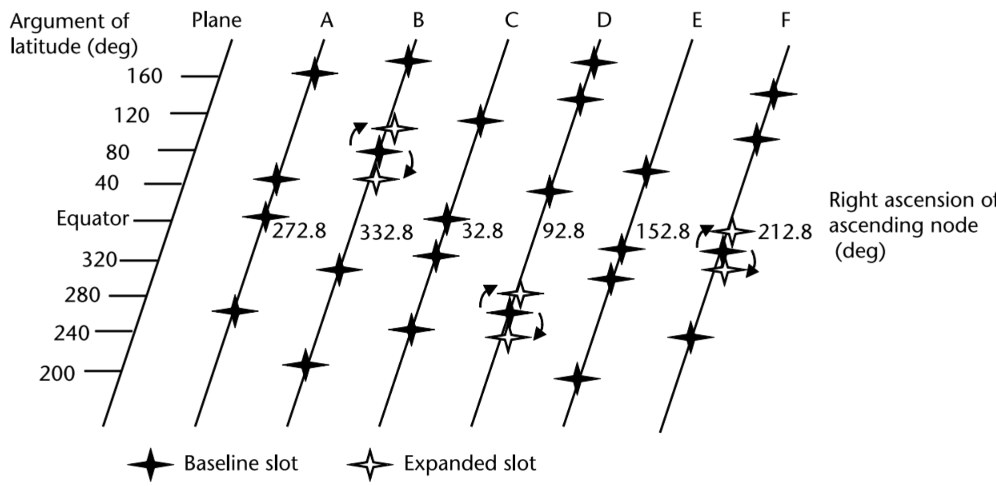

FIGURE 1.3: Depiction of the arrangement of satellites in the 24 slot configuration (baseline slots) and the expanded 24 slot configuration [3].

clock phase that is determined by a weighted average of many H-maser clocks on site. Station AMC2 in Colorado Springs, Colorado, is an H-maser based station operated by USNO that is loosely steered to the master clock using a satellite link. In both cases, USN3 and AMC2 have their data calibrated for cable delays, with AMC2 loosely steered to USN3, so that they are synchronized at the ns level. Therefore it is particularly useful that one of these stations be used as a reference clock in the system, with the other acting as a stability check on the GPS network solution. Other H-maser based stations of varying quality and characteristics are shown around the globe (Fig. 1.4). Some H-maser stations are problematic in that the clock phases are known to jump frequently (e.g., station IRKT). However, there is a sufficient number (at least 8) high-quality H-maser based stations to detect the passage of a 1 ns clock phase anomaly through the global network.

1.2.3 Solutions and Software

To perform the necessary computations for the complicated positioning networks, JPL developed the GNSS-Inferred Positioning System and Orbit Analysis Simulation Software

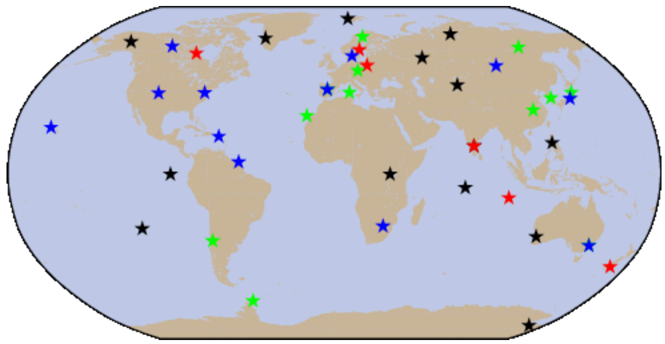

Figure 1.4: The 40-station global GPS network of Earth-based stations acquiring 1 s dual-frequency carrier phase data, indicating clock type. Blue stars are H-masers, red are Rb, green are Cs, and black are quartz.

(GIPSY-OASIS, or commonly just referred to as GIPSY). As of 2018, the next-generation GipsyX software has taken over processing and has re-processed all previous data, and is proposed to be used here. GIPSY has been validated by a series of high precision NASA missions over the last decade (e.g., GRACE, TOPEX, JASON) that have required spacecraft positioning at the cm level, timing at the < 0.1 ns level, and station positioning at the few-mm level. GIPSY and new GipsyX software are licensed to UNR for research purposes.

Each of the high-quality receiver stations of Fig. 1.4 provide raw GPS data at 1 s intervals in standard Receiver Independent Exchange Format (RINEX) files that are distributed by the NASA Crustal Dynamics Data Information System (CDDIS) archive, as part of the International GNSS Service (IGS). Note that several of these ground stations are disciplined by atomic clocks, which could themselves be made part of the atomic clock sensor network together with those in orbit. At every second, a file from each station is generated that contains data from all GPS satellites in view, which is typically 6–10. Having sufficient coverage from a network such as this guarantees that every GPS satellite is in view of several ground stations at the same time. This ensures that the broadcast microwave signals can be effectively transferred between the space and control segments, which allows the relative clock phase to be determined with < 0.1 ns precision. At every 1 s epoch, the RINEX files contain 4 key measurements, including a carrier phase and a pseudorange at both L1 and L2 frequencies, thus allowing for calibration of $\sim$ 10 ns amplitude ionospheric delay with $\sim$ 0.01-ns accuracy. Pseudorange is typically measured with $\sim$ 2 ns precision. In contrast, carrier phase is measured with $\sim$ 0.02-ns precision. The Combination of the 4 observables allow for robust detection of data outliers and cycle slips in the integer bias, and enable robust integer ambiguity resolution [5, 6].

The GipsyX software takes the observables from each network station and uses least-squares to estimate the final solutions. The algorithm can be considered in three stages:

1. Pre-processing of the data to detect and repair common problems

2. Accurate modeling of the observables

3. Inversion of model parameters

The GipsyX software models abide by the conventions of the International Earth Rotation and Reference Frame Service (IERS), using standard antenna and inter-channel bias calibrations approved and distributed by IGS [7]. Included in the IERS standards is the conventional treatment of relativistic modeling of the GPS satellite clocks, accounting for variation in satellite velocity and gravitational potential due to small orbit eccentricity, resulting in a semi-diurnal sinusoidal signal of $\sim$ 30 ns amplitude. The frequency of the GPS clocks are intentionally set slower to account for the mean effects of relativity (-38 μs per day) and Shapiro delay (< 0.1 ns) on the signals as they traverse the Earth's gravitational potential. Residual relativistic effects are dominated by Earth flattening (also known as the J2 effect), resulting in a 6 hour periodic signal of amplitude $\sim$ 0.07 ns [8].

GipsyX contains a sophisticated least-squares estimator, similar conceptually to the Kalman Filter. Tropospheric delay is modeled using state-of-the-art global mapping function that relates zenith delay to any elevation and azimuth, depending on geographic location and time of year. The zenith delay and two gradient parameters are then estimated as a random walk process using the GPS data from each station. By this method, tropospheric delay can be modeled at the few-mm level, corresponding to ~ 0.01 ns. As stated before, station positions can be estimated at the few-mm level, but if the goal is to estimate satellite and station clocks, it is sufficient (and more robust to detect problem data) to fix station positions at their known reference frame coordinates at the epoch of measurement. These coordinates are typically known at the few millimeter level, corresponding to ~ 0.01 ns.

The GipsyX software models the GPS satellite orbits in the ECI (Earth-centered inertial) frame, which is aligned to the International Celestial Reference Frame (ICRF). The solid Earth is modeled in the ECEF (Earth-centered Earth-fixed) frame, co-rotating with the Earth. Short-term motions of the solid Earth surface are dominated by solid Earth tides at the 0.5-m (< 2 ns) level at semi-diurnal period. Known motions of the solid Earth surface including solid Earth tides and ocean tidal loading are typically modeled with millimeter accuracy, corresponding to < 0.01 ns. Connecting ECEF to ECI is Earth orientation, modeled as a combination of precession, nutation, polar motion, and rotation. Of these, polar motion and length of day are the least predictable, and must be measured continuously. GipsyX can estimate polar motion and length of day from the GPS data to within a few mm at the Earth's surface, corresponding to ~ 0.01 ns. Once all of this modeling is complete, the final solutions are published by JPL to the public within a week of the day being estimated.

1.2.4 Data from JPL

As mentioned before, high-quality timing data for nearly the past two decades are publicly available and are routinely updated at 30 s intervals. However, there are now several hundred GPS stations around the globe that produce raw GPS carrier phase measurements at 1 s intervals, which provides a much finer time resolution of possible events, and increases the discrete Fourier transform frequency range substantially. Such high rate data are not publicly available, hence we have to generated them ourselves and with the help of JPL.

There are several types of data regarding GPS that are processed and made available by JPL. There are 3 tiers of access, ultra-rapid, rapid, and final. Ultra-rapid is updated 4 times per day with relatively low quality solutions but fast turn-around. Rapid is a daily solution that is available 17 hours after every UTC day and is of higher quality. The type we are generally interested in is final, which is released 13 days after the end of the solution week and is of the highest quality. Within the released data is several different files that serve different purposes like details on which satellites were in the shadow of the Earth for example. The files we are concerned with are the satellite atomic clock time-series bias data and the Cartesian positions of the satellites.

For our purposes, it is convenient to use satellite orbits that have already been determined by JPL at 15-minute intervals. Since orbits are smooth in nature, interpolation can be achieved with sub-mm (0.01 ns) error. The orbit positions themselves have an estimated accuracy of 1-2 cm, corresponding to < 0.1 ns error. Whereas satellite orbit positions are a dominant error source, it should be kept in mind that these errors have a very long time variation compared to the $\sim\ 1,000\,\mathrm{s}$ event time windows that will be proposed in later sections. Satellite and station clocks are all estimated as a white noise process, so that the estimated clock phase is entirely driven by the data with no a priori constraints. One clock is held fixed (un-estimated) as a reference clock, as the data are only sensitive to relative time.

1.3 Motivation

This work is based on the possibility that exotic light fields may cause apparent variations of the fundamental constants of nature. Such variations in turn lead to shifts in atomic energy levels, which may be measurable by monitoring atomic frequencies [9]. Such monitoring is performed naturally in atomic clocks, which tell time by locking the frequency of externally generated electromagnetic radiation to atomic frequencies. Here, we propose to analyze time as measured by atomic clocks on-board GPS satellites to search for event-induced transient variations of fundamental constants. In effect we use the GPS constellation as a $\sim 50,000\,$km-aperture exotic physics detector. We will be able to search for exotic physics events in any time window over ~ 20 years, such as those co-incident with known astrophysical events, and establish means for continuous monitoring of GPS for these events in the future. Using the GPS network as an observatory for exotic physics is the main objective of the GPS.DM group.

Chapter 2

Coupling to Atomic Clocks

2.1 Mathematical Formalism

This section serves as a brief introduction to the mathematical tools used to describe the Standard Model of elementary particles. To include relativistic dynamics, it is useful to think of space and time as one 4-dimensional entity. A signal point in space-time is known as an event, and it is represented as a four-vector x^μ with the indices $\mu = 0, 1, 2, 3$. The zeroth entry of the vector corresponds to the temporal component of the vector with the nonzero indices being the spatial components. An event vector for example contains first the time of the event, then the 3 dimensional position of the event,

$$x^\mu = (ct, \vec{x})\,. \tag{2.1}$$

In Special Relativity, the 4-D space-time is non-Euclidean, that is to say that dot-products do not act the same as they do in a Euclidean space. They act according to the space-time metric,

$$\eta_{\mu\nu} = \begin{pmatrix} 1 & 0 & 0 & 0 \\ 0 & -1 & 0 & 0 \\ 0 & 0 & -1 & 0 \\ 0 & 0 & 0 & -1 \end{pmatrix} . \tag{2.2}$$

The metric is used to raise or lower 4-vectors. Vectors with an upper index are called contravariant, while lower indices indicate covariant vectors. To switch between the two vector types, you can sum over one of the indices of the metric,

$$x_\nu = \eta_{\mu\nu} x^\mu \,, \tag{2.3}$$

where the repeated index μ implies a sum over the range of that index (one of the repeated indices must be an upper, while the other is a lower). Note that the resulting 4-vector x_ν now has the opposite sign in the spatial part, hence

$$x_\nu = (ct, -\vec{x}) \,. \tag{2.4}$$

We can now take a sum over these contravariant and covariant vectors, which defines the dot product in space-time,

$$x_\mu x^\mu = (ct)^2 - \vec{x} \cdot \vec{x} \,. \tag{2.5}$$

Derivatives in this formalism are written in a compact way. A derivative with respect to the μ^{th} component is written with a single ∂_μ. Note that though it is written as a covariant vector, it does not have an opposite sign in the spatial component,

$$\partial_\mu \equiv \frac{\partial}{\partial x^\mu} \,. \tag{2.6}$$

Another important convention is the definition of the gamma matrices, defined as

$$\gamma^0 \equiv \begin{pmatrix} I & 0 \\ 0 & -I \end{pmatrix} \quad \vec{\gamma} \equiv \begin{pmatrix} 0 & \vec{\sigma} \\ -\vec{\sigma} & 0 \end{pmatrix}, \tag{2.7}$$

where each element represents a 2x2 matrix with I denoting the identity matrix and σ denoting the conventional Pauli spin matrices.

2.2 Fundamental Constant Variation

The Standard Model Lagrangian that describes the proton, electron, and electromagnetic fields is then

$$\mathcal{L}_{SM} = \sum_{j=e,p} \bar{\psi}_j (i\hbar c \partial_\mu \gamma^\mu - m_j c^2)\psi_j - ecA_\mu \bar{\psi}_j \gamma^\mu \psi_j - \frac{1}{4} F_{\mu\nu} F^{\mu\nu} , \tag{2.8}$$

where ψ_e (ψ_p) is the 4-component wavefunction of the electron (proton), e is the elementary charge, and A_μ is the electromagnetic 4-potential, with the Faraday tensor defined as $F_{\mu\nu} = \partial_\mu A_\nu - \partial_\nu A_\mu$. Here and below we use the rationalized Lorentz-Heaviside unit system for electromagnetism. GPS.DM is interested in the addition of the following interaction terms to this Lagrangian, with some exotic scalar field ϕ,

$$\mathcal{L}_{int} = \left[-\Gamma_e m_e c^2 \bar{\psi}_e \psi_e - \Gamma_p m_p c^2 \bar{\psi}_p \psi_p + \frac{1}{4} \Gamma_\alpha F_{\mu\nu} F^{\mu\nu} \right] \phi, \tag{2.9}$$

where the Γ_X are the associated couplings constants. This is also known as the linear scalar portal to standard model particles. We use a linear coupling to ϕ as an example here, but the results are easily changed to the case of a quadratic coupling, as is demonstrated in later chapters. The combination $\Gamma_X \phi$ is dimensionless. The addition of these terms leads to the total Lagrangian,

$$\mathcal{L} = \sum_{j=e,p} \bar{\psi}_j(i\hbar c\partial_\mu\gamma^\mu - m_j c^2(1+\Gamma_j\phi))\psi_j - ecA_\mu\bar{\psi}_j\gamma^\mu\psi_j - \frac{1}{4}(1-\Gamma_\alpha\phi)F_{\mu\nu}F^{\mu\nu} \ . \tag{2.10}$$

From inspection, we can immediately make the interpretation of changing electron and proton masses, but the scaling for α is not immediately obvious. To understand this, we can make the following gauge transformation

$$A_\mu \to \frac{e}{c(1-\Gamma_\alpha\phi)}\tilde{A}_\mu. \tag{2.11}$$

To understand what difference this will make, we must see how the factor $F_{\mu\nu}F^{\mu\nu}$ scales with this change,

$$\begin{aligned} F_{\mu\nu}F^{\mu\nu} &= (\partial_\mu A_\nu - \partial_\nu A_\mu)(\partial^\mu A^\nu - \partial^\nu A^\mu) \\ &= \partial_\mu A_\nu\partial^\mu A^\nu - \partial_\mu A_\nu\partial^\nu A^\mu - \partial_\nu A_\mu\partial^\mu A^\nu + \partial_\nu A_\mu\partial^\nu A^\mu \\ &= 2(\partial_\mu A_\nu\partial^\mu A^\nu - \partial_\mu A_\nu\partial^\nu A^\mu)\,. \end{aligned} \tag{2.12}$$

Once we plug in our gauge transformation into this expression, we will encounter derivatives of the field ϕ, for example,

$$\partial_\mu\left(\frac{\tilde{A}_\nu}{(1-\Gamma_\alpha\phi)}\right) = \frac{\partial_\mu\tilde{A}_\nu}{(1-\Gamma_\alpha\phi)} + \Gamma_\alpha\frac{\tilde{A}_\nu\partial_\mu\phi}{(1-\Gamma_\alpha\phi)^2} \ . \tag{2.13}$$

Due to our interest in ultralight fields, which is equivalent to requiring that the field ϕ oscillates very slowly over space and time, we make the argument that derivatives in the electromagnetic vector field are much larger than those of the ϕ field on the scale of an atom, or $\partial_\mu \phi / \partial_\mu \tilde{A}_\nu \ll 1$, so we neglect that term. The relation then simplifies to

$$\mathcal{L} = \sum_{j=e,p} \bar{\psi}_j (i\hbar c \partial_\mu \gamma^\mu - m_j(1+\Gamma_j \phi)c^2)\psi_j - \alpha(1-\Gamma_\alpha\phi)^{-1}\hbar c \tilde{A}_\mu \bar{\psi}_j \gamma^\mu \psi_j - \alpha(1-\Gamma_\alpha\phi)^{-1}\frac{\hbar/c}{4}\tilde{F}_{\mu\nu}\tilde{F}^{\mu\nu}\,, \quad (2.14)$$

using the definition of the fine structure constant in this unit system $\alpha = e^2/\hbar c$.We are now free to make the interpretation that for slowly oscillating fields, these interaction terms vary fundamental constants like

$$m_{e,p} \rightarrow m_{e,p}(1+\Gamma_{e,p}\phi)\,, \quad (2.15)$$

$$\alpha \rightarrow \frac{\alpha}{(1-\Gamma_\alpha\phi)} \approx \alpha(1+\Gamma_\alpha\phi)\,. \quad (2.16)$$

In the following chapters, we will use these results to show how linear or quadratic couplings to the standard model particles and fields can directly affect atomic transition frequencies based on such variation of fundamental constants.

Chapter 3

Exotic Light Fields

3.1 Introduction

Multimessenger astronomy, a subject in which different classes of signals originating from the same astrophysical event are observed, provides a wealth of information about astrophysical processes with far-reaching implications [10]. The conventional focus of multimessenger astronomy has been to search for signals from known fundamental forces and standard model particles: electromagnetic waves, neutrinos, cosmic rays, and gravitational waves (GWs) (Table 3.1).

Beyond searching for signals like GWs that are predicted by well-substantiated theories like general relativity, other sensor networks [11] could be used to search for astrophysical signals predicted by different theoretical models [12]. Could exotic light fields (ELFs) produced by cataclysmic astrophysical events be directly observed using atomic clocks [13, 14]?

Here we address this question by considering detection of ELFs associated with gravitational wave events [15–17], estimating signal amplitudes, delays, rates, and distances of sources to which global clock networks could be sensitive. This discussion is followed in the next chapter by a proof-of-principle demonstration based on analysis of data from the network of atomic clocks comprising the global positioning system (GPS) with the GPS.DM Observatory [13, 18–20]. We find in this chapter that networks of clocks can act as ELF telescopes to detect signals from sources that produce ELF bursts of sufficient intensity, and if ELFs exist, they could act as additional messengers for astrophysical events.

3.2 Physical Description of ELFs

Many of the great mysteries of modern physics suggest the existence of exotic fields with light quanta (masses $\ll 1$ eV): the nature of dark matter [21–25] and dark energy [26–28], the hierarchy problem [29], the strong-CP problem [30–36], and the search for a quantum theory of gravity [37–39]. Intense bursts of such ELFs could be generated by cataclysmic astrophysical events such as black hole or neutron star mergers (NSM) [40, 41], supernovae [42, 43], or other phenomena, such as the processes that produce fast radio bursts (FRBs) [44, 45]. Due to the small masses being considered for ELFs, a high energy event may not be required for the production of ELFs, but may allow for enough released energy in a burst of ELFs for them to become detectable.

Similar to antennae used to detect radio waves and interferometers used to detect GWs, atomic clocks are sensitive to coherent, classical waves and are not suitable for detection of individual particles. This is in contrast to detectors such as those employed in observations of cosmic neutrinos [46], gamma rays [47, 48], and searches for weakly interacting massive particles (WIMPs) [49, 50]. The key point is that in order to be detectable by atomic clocks, the astrophysical source must produce coherent ELF waves with high mode occupation numbers. Thus we focus our attention on coherent production mechanisms for ELFs [40, 41, 51, 52] rather than thermal production mechanisms as considered in previous analyses [42, 43].

Event Type	Electromagnetic	Cosmic Rays	GWs	Neutrinos	Event Name
Solar Flare	✓	✓	-	•	SOL1942-02-28 [53]
Supernova	✓	•	•	✓	SN 1987A [54]
NSM	✓	-	✓	•	GW170817 [10]
Blazar	✓	•	-	✓	TXS 0506+056 [55]

Table 3.1: Observed (✓) and predicted (•) signals from astrophysical multimessenger events.

Atomic clocks can detect ELFs that effectively alter fundamental constants [13] using so-called "portals" through which ELFs can interact with standard model particles and fields [12], as discussed in the previous chapter. The coupling strength determines, for a given ELF intensity, the relative signal amplitude detected by the particular sensor. Astrophysical observations and laboratory experiments set constraints on the coupling strengths between ELFs and standard model particles and fields [12]. To estimate the potential astrophysical reach of clock networks, we assume the largest coupling of ELFs to standard model particles consistent with existing astrophysical and laboratory constraints and then calculate the distance to a source for which the signal size is just detectable given an energy release in the form of ELFs. Gravitational wave events can radiate large amounts of energy, a fraction of which could be emitted in the form of ELFs. For example, black holes may be surrounded by dense clouds of exotic bosons that could lead to ELF bursts coincident with gravitational wave emission [41, 56–59].

3.2.1 ELF flux from an astrophysical event

Instead of invoking a specific model-dependent ELF production mechanism, given that we are evaluating a generic search for exotic physics, we assume that some amount ΔE of the total energy emitted by the astrophysical event is converted into an ELF. For concreteness, we assume that the initial emitted ELF is a spin-0 field $\phi(r, t)$ described by the Klein-Gordon equation,

$$\frac{1}{c^2}\frac{\partial^2}{\partial t^2}\phi - \nabla^2\phi + \frac{m^2c^2}{\hbar^2}\phi = 0\,. \tag{3.1}$$

This has spherically symmetric wave solutions,

$$\phi(r,t) = \frac{A_0}{r}\cos\left(k_0 r - \omega_0 t\right), \tag{3.2}$$

where A_0 is the initial ELF amplitude, r is the radial coordinate, ω_0 is the initial ELF frequency, and k_0 is the initial wavevector. Although we assume spherical symmetry, these results are readily generalized. We are defining these quantities in terms of initial values due to the dispersion such a matter wave will experience upon propagation (Section 3.2.3). Here and below we are focusing on the fields outside the gravitational potential of the source, with all the initial quantities referring to the values just outside the potential.

In order for the ELF burst to be correlated with astrophysical observations in electromagnetic or gravitational wave modalities, we must require that the field is ultra-relativistic: $\omega_0 \approx ck_0$. To understand what the energy density of an ELF pulse near the Earth is, we envoke the definition of the energy density for a free field:

$$\rho = \frac{1}{2c^2}\dot{\phi}^2 + \frac{1}{2}(\nabla\phi)^2 + \frac{1}{2}\frac{m^2c^2}{\hbar^2}\phi^2\ . \tag{3.3}$$

In the vicinity of the center of the ELF pulse, the model Eq. (3.2) can be considered instead with the amplitude near the Earth of A. The energy density is then

$$\begin{aligned}\rho = \frac{A^2}{2r^2}\frac{\omega_0^2}{c^2}\Bigg[\sin^2(\omega_0 t - k_0 r) + \left(\frac{ck_0}{\omega_0}\right)^2 \sin^2(\omega_0 t - k_0 r)\\ + \left(\frac{mc^2}{\hbar\omega_0}\right)^2 \cos^2(\omega_0 t - k_0 r)\Bigg] + \mathrm{O}\left(\frac{1}{r^3}\right)\ ,\end{aligned} \tag{3.4}$$

where we will neglect terms of order $1/r^3$. Taking the ultra-relativistic limit, $\omega \approx ck \gg mc^2/\hbar$, and taking the time average, the energy density for a free spin-0 field is then given by:

$$\langle \rho \rangle \approx \frac{1}{2}\left(\frac{A}{r}\frac{\omega_0}{c}\right)^2 . \tag{3.5}$$

To relate this to the total energy emitted into ELFs (ΔE), we assume that the ELF pulse has an initial temporal duration of τ_0, a duration at the Earth of τ, and is well-localized, $c\tau \ll r$. The energy density is then

$$\rho \approx \frac{\Delta E}{4\pi r^2 c\tau} . \tag{3.6}$$

Combining the two previous equations yields the ELF amplitude at the Earth,

$$A \approx \frac{1}{\omega_0}\sqrt{\frac{c\Delta E}{2\pi\tau}} , \tag{3.7}$$

with A_0 defined in terms of τ_0. The detectable ranges of ELF frequencies ω and Earth burst durations τ are set by the characteristics of the sensor network.

The radiated energy in the form of GWs from recently observed black hole mergers is a few $M_\odot c^2$ [15, 16], whereas for recently observed neutron star mergers the radiated energy in the form of GWs is $\gtrsim 0.025 M_\odot c^2$ [17], where only a lower bound on energy release is obtained due to uncertainty about the equation of state for the neutron stars. For the purposes of the following sensitivity estimates, we assume that it may be possible to have $\Delta E \sim M_\odot c^2$ of energy released in the form of ELFs from a black hole merger and $\Delta E \sim 0.1 M_\odot c^2$ of energy released in the form of ELFs from a neutron star merger.

3.2.2 ELF burst delay

To correlate an ELF signal observed in the sensor networks to the known time of an astrophysical event, we need to consider when we would expect to see an ELF signal relative to the standard signal (e.g., an electromagnetic or gravitational wave). For simplicity, prompt emission of the ELF from the source is assumed (coincident with, for example, the gravitational wave emission). If the delay in time between the arrival of an electromagnetic signal and the ELF signal is δt, the distance to the source of the event is R, and the center of the ELF pulse travels at group velocity $v_g < c$, then

$$\delta t = R\left(\frac{1}{v_g} - \frac{1}{c}\right) . \tag{3.8}$$

Since $c\delta t$ is the light travel distance during the delay time and is much smaller than the distance to the source (i.e., $c\delta t/R \ll 1$), we can rearrange this and approximate as

$$v_g = \frac{c}{(1 + c\delta t/R)} \approx c\left(1 - \frac{c\delta t}{R}\right) , \tag{3.9}$$

which ensures that the ELF must travel at ultra-relativistic speeds. Searching for ELF signals occurring within δt of the astrophysical event constrains the observable ELF particle mass, since there is a relationship between v_g and the Compton frequency of the field through the dispersion relation. A search for ELFs, like many oscillating dark matter (DM) searches, would probe the oscillation frequency of the field ω. The total energy of the particle traveling with velocity v_g is $\hbar\omega_0 = \gamma mc^2$ where γ is the Lorentz factor. Then, using the same approximation as in Eq. (3.9),

$$\omega_0 = \frac{mc^2}{\hbar}\left[1 - \left(1 + \frac{c\delta t}{R}\right)^{-2}\right]^{-\frac{1}{2}} \approx \frac{mc^2}{\hbar}\sqrt{\frac{R}{2c\delta t}} . \tag{3.10}$$

To illustrate the effect of the delay on the observable particle mass m, Fig. 3.1 shows the accessible parameter space for an ELF associated with the GW170608 binary black hole coalescence event [60] in terms of m and signal frequency $\omega/(2\pi)$. This assumes a requirement that $\delta t \leq 10$ hours, due to the limit of available data that we can search.

3.2.3 ELF burst duration and dispersion

An important point in analyzing the sensitivity of sensor networks to ELF pulses is the dispersion of the pulse as it propagates from the source to the Earth. As noted above, if we assume the ELF is a massive scalar/pseudoscalar field, it is described by the Klein-Gordon equation, which yields the dispersion relation:

$$\omega(k) = \sqrt{(ck)^2 + \left(\frac{mc^2}{\hbar}\right)^2} \ . \tag{3.11}$$

This allows us to find an expression for the group velocity as a function of k, since $v_g(k) = \partial\omega/\partial k$, so

$$v_g(k) = c\left(\frac{ck}{\omega(k)}\right) \ . \tag{3.12}$$

Assuming for simplicity that at the source the generated signal is Fourier limited, then the spread of frequencies $\Delta\omega$ in the ELF signal is

$$\Delta\omega \approx \frac{1}{\tau_0} \ , \tag{3.13}$$

As can be seen by differentiating the group velocity [Eq. (3.12)] with respect to the wave vector k at the center of the pulse, the group velocity for different wavevectors is

$$\Delta v_g \approx \Delta k \left.\frac{\partial^2\omega}{\partial k^2}\right|_{k_0} \approx \left(\frac{mc^2}{\hbar\omega_0}\right)^2 \frac{1}{k_0\tau_0} \ . \tag{3.14}$$

Since the ELF is ultra-relativistic, it is reasonable to make the approximation $k_0 \approx \omega_0/c$, and so the duration of the ELF burst as detected on Earth would be

$$\tau \approx \frac{R\Delta v_g}{c^2} \approx \frac{R}{c}\left(\frac{mc^2}{\hbar\omega_0}\right)^2 \frac{1}{\omega_0\tau_0} \ . \tag{3.15}$$

The characteristics of the clocks used in the ELF telescope sensor networks impose some practical limitations on the observable values of τ and ω, and through Eq. (3.15), limits the range of observable masses. To illustrate these limitations, Fig. 3.1 shows the accessible parameter space for an ELF associated with the GW170608 binary black hole coalescence event [60] in terms of particle mass m and signal frequency $\omega/(2\pi)$ assuming a requirement that $\tau \leq 10$ hours.

To get an understanding of what a potential ELF signal might look like, we can take a Taylor expansion of $\omega(t)$ around the time the center of the pulse arrives at Earth, $t_s = R/v_g$.

$$\begin{aligned}\omega(t) &\approx \omega(t_s) - \left.\frac{\Delta\omega}{\Delta t}\right|_{t_s}(t - t_s) \\ &\approx \omega_0 - \frac{1}{\tau_0\tau}(t - t_s) \ . \end{aligned} \tag{3.16}$$

The sign of the linear term comes from our knowledge that due to the group velocity relationship [Eq. (3.12)], higher frequencies will arrive first, and lower ones last. The validity of this approximation follows from the results in Section 3.2.4. The pulse will then have the approximate temporal form at the Earth,

$$\phi(R,t) \approx \frac{A_0}{R}\sqrt{\frac{\tau_0}{\tau}}\exp\left(-\frac{(t-t_s)^2}{2\tau^2}\right)\cos\left(\omega_0(t-t_s) - \frac{1}{2\tau_0\tau}(t-t_s)^2\right) \ . \tag{3.17}$$

Due to the time dependence on the frequency, the ELF signal will be seen as an “anti-chirp" at a detector. The above model allows us to predict what this signal will look like if we sample it in a similar manner to that of the proposed detector network, as demonstrated by

Fig. 3.2.

3.2.4 Derivation of Matter Wave Pulse Propagation

Any type of wave will disperse upon propagation as long as the dispersion relation $\omega(k)$ [Eq. (3.11)] has a nonzero second derivative with respect to k. This ensures that the group velocity is a function of k. We can gain some insight into how this works for the case of matter waves by deriving a more rigorous result than the treatment in Section 3.2.3. We will assume the the waves are spherically symmetric and define $\phi(r,t) = u(r,t)/r$ so that $u(r,t)$ satisfies the 1D wave equation. The general solution to the 1D wave equation is an integral over the Fourier amplitudes $A(k)$ of each k-value wave component,

$$u(r,t) = \frac{1}{\sqrt{2\pi}} \mathrm{Re}\left[\int_{-\infty}^{\infty} A(k) e^{i(kr-\omega(k)t)} dk\right] , \tag{3.18}$$

with the dispersion relation $\omega(k)$ for relativistic particles given by (3.11). The initial conditions define the Fourier amplitudes [61]

$$A(k) = \frac{1}{\sqrt{2\pi}} \int_{0}^{\infty} e^{-ikr} \left[u(r,0) + \frac{i}{\omega(k)} \frac{\partial u}{\partial t}(r,0)\right] dr , \tag{3.19}$$

with $u(r,0)$ and $\partial u/\partial t(r,0)$ being the initial values near the source. For this example, we will use initial conditions specified by [61] for a plane wave pulse with initial wave amplitude A_0, initial spatial width L_0, and initial wavevector k_0:

$$\begin{aligned} u(r,0) &= A_0 e^{-r^2/(2L_0^2)} \cos(k_0 r) , \\ \frac{\partial u}{\partial t}(r,0) &= 0 . \end{aligned} \tag{3.20}$$

These initial conditions result in two pulses traveling in opposite directions, but we will only focus on the forward propagating pulse with the Fourier amplitude

$$A(k) = \frac{A_0 L_0}{2} e^{-(L_0^2/2)(k-k_0)^2} \ . \tag{3.21}$$

We can approximate $\omega(k)$ as a Taylor expansion around k_0 to second order as

$$\omega(k) \approx \omega_0 \left[1 + \frac{v_g}{\omega_0}(k - k_0) + \frac{L_0 \Delta v_g}{2\omega_0}(k - k_0)^2 \right] \ , \tag{3.22}$$

with the inserted definitions from Eq. (3.12) and Eq. (3.14). The second term above is of the order $(k_0 L_0)^{-1}$ which reflects our requirement that the initial wavelength of the field is much less than the initial spatial spread (i.e. $\lambda_0 \ll L_0$). The third term above is of the order $(c\delta t/R)(k_0 L_0)^{-2}$ which like the preceding term and the approximation from Eq. (3.9) is $\ll 1$, which justifies this approximation for $\omega(k)$. This allows the integral in (3.18) to be evaluated in a closed form, and the final solution for $\phi(r,t)$ is

$$\phi(r,t) \approx \frac{A_0}{r} \sqrt{\frac{\tau_0}{\tau(t)}} \exp\left(-\frac{(t - r/v_g)^2}{2\tau(t)^2} \right) \cos\left(\varphi(r,t)\right) \ . \tag{3.23}$$

with time dependent temporal spread $\tau(t)$ defined as

$$\tau(t) = \sqrt{\tau_0^2 + \left(\frac{\Delta v_g t}{v_g} \right)^2} \ , \tag{3.24}$$

and we have substituted $L_0/v_g = \tau_0$. From this we can see that at large t, the temporal spread increases linearly with time as $(\Delta v_g/v_g)t$. The phase argument of the oscillatory part is given by

$$\varphi(r,t) = (\omega_0 t - k_0 r) - \frac{1}{2\tau(t)^2} \frac{\Delta v_g t}{v_g \tau_0} (t - r/v_g)^2 + \frac{1}{2} \tan^{-1}\left(\frac{\Delta v_g t}{v_g \tau_0} \right) \ . \tag{3.25}$$

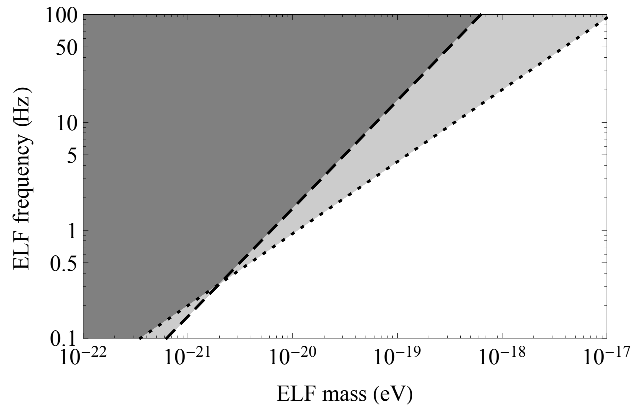

FIGURE 3.1: For the distance ($\approx 10^9$ ly) and source duration (≈ 1 s) of the GW170608 binary black hole coalescence event [60] and a maximum delay and duration of ≈ 10 hours, the dark grey shaded region represents the accessible parameter space for ELF mass and frequency for detection by the GPS constellation. The dashed line is the constraint from delay [Eq. (3.10)] and the dotted line is the constraint from dispersion [Eq. (3.15)].

We can see that (3.23) has a wave amplitude that depends on $\tau(t)^{-1/2}$, just as in the estimate in Eq. (3.7). It can also be shown that the time derivative of (3.25) approximates to Eq. (3.17) for $r = R$, near $t = R/v_g$.

3.3 GPS as an ELF telescope

3.3.1 Clock Data Processing

The data given in a GPS time-series dataset represents the bias between a reference clock's phase and a network clock's phase, measured in nanoseconds. The Earth-based station measures the carrier phase of the satellite clocks at each sampling time (or epoch) and it is then calculated relative to the chosen reference clock. The phase bias for each data point for the a^{th} network clock and j^{th} epoch can be represented as an integral over the bias in

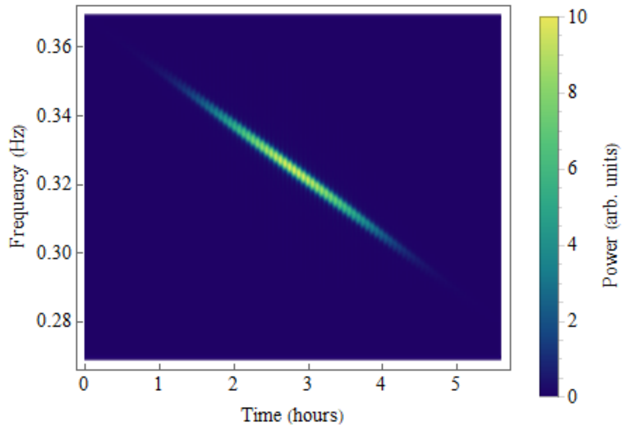

FIGURE 3.2: Simulated example of an ELF signal in time-frequency space. This reflects the model Eq. (3.17), with an ELF mass of $m = 10^{-20}$ eV and the initial conditions $\delta t = 10$ hours, $\tau_0 = 10$ s, and $R = 40$ Mpc. These choices of parameters allow this signal to exist in a frequency range accessible by the GPS.DM sensor network.

fractional frequency excursions:

$$d_{a,j}^{(0)} = \int_0^{t_j} \left(\frac{\delta\nu_a(t')}{\nu_a} - \frac{\delta\nu_r(t')}{\nu_r} \right) dt' \,, \tag{3.26}$$

where ν_a and ν_r are the a^{th} and reference clock's frequency respectively. As can be seen in later sections, it will become useful to isolate the a^{th} clock's fractional frequency excursion. If we preform first order differencing on these data, we can approximate the integral as a single-term midpoint-based Riemann sum:

$$\begin{aligned} d_{a,j}^{(1)} &= d_{a,j+1}^{(0)} - d_{a,j}^{(0)} \\ &= \int_0^{t_{j+1}} \left(\frac{\delta\nu_a(t')}{\nu_a} - \frac{\delta\nu_r(t')}{\nu_r} \right) dt' - \int_0^{t_j} \left(\frac{\delta\nu_a(t')}{\nu_a} - \frac{\delta\nu_r(t')}{\nu_r} \right) dt' \\ &= \int_{t_j}^{t_{j+1}} \left(\frac{\delta\nu_a(t')}{\nu_a} - \frac{\delta\nu_r(t')}{\nu_r} \right) dt' \\ &\approx \left(\frac{\delta\nu_a(\bar{t}_j)}{\nu_a} - \frac{\delta\nu_r(\bar{t}_j)}{\nu_r} \right) T \,. \end{aligned} \tag{3.27}$$

with $\bar{t}_j = (t_{j+1} + t_j)/2$ being the temporal midpoint between the two epochs and T being the sampling interval duration.

This still leaves the reference clock term, so we can further refine these data by defining the weighted average over all clocks, $\bar{d}_j^{(1)}$. Every clock dataset will contain the same reference clock term above, so by averaging over all clocks in the network, we will sum over the same reference clock contributing terms. The average will then approximately cancel out contributions from the network clocks and leave only contributions from the reference clock,

$$\bar{d}_j^{(1)} = \frac{\sum_a d_{a,j}^{(1)}(\sigma_a)^{-2}}{\sum_a (\sigma_a)^{-2}} \approx -\frac{\delta\nu_r(\bar{t}_j)}{\nu_r} T \,, \tag{3.28}$$

where σ_a is the standard deviation of the a^{th} clock. We can then subtract this weighted average from each of the network time series and divide by the sample interval to get contributions from only the a^{th} clock:

$$\frac{d_{a,j}^{(1)} - \bar{d}_j^{(1)}}{T} \approx \frac{\delta\nu_a(\bar{t}_j)}{\nu_a} \,. \tag{3.29}$$

This result now contains the intrinsic device clock frequency noise, linear clock frequency drifts, and potentially new physics. This can be quite useful for determining and analyzing frequency excursion signals that may only apply to one clock or a subset of clocks in the network. As we are considering analyzing data after this stage of pre-processing, we denote it simply as $d_{a,j}$.

3.3.2 Sensitivity of clock networks

We can now derive the sensitivity of a clock network to ELFs. From [20], the Bayesian likelihood for a given model M of a deterministic signal $s_{a,j}$ to exist in the datastream $d_{a,j}$ is modeled by a multivariate Gaussian distribution. We will consider the data and the signal in frequency space due to our interest in an oscillating signal, so the index j will get replaced with p which indexes the frequency after taking the discrete Fourier transform with N data points. While the signal exists, N_w statistically significant sub-windows of data will be treated separately, each with a central window time of t_w, where a frequency model $f(t_w)$ will be checked against the data ($f(t_w) = \omega(t_w)/2\pi$ from Eq. 3.16 for example). The form of the frequency space likelihood distribution for this search is derived from [20],

$$\mathcal{L}(\mathbf{d}|M) = \frac{1}{\det(2\pi\tilde{\boldsymbol{C}})} \prod_{p\in f_p} \exp\left(-\frac{1}{2}\chi_p^2\right),$$
$$\chi_p^2 = 2\sum_{a}^{N_d} \frac{\left|\tilde{d}_{a,p} - \tilde{s}_{a,p}\right|^2}{\tilde{C}_p}\ , \tag{3.30}$$

where I have assumed p does not index the Nyquist or dc frequencies. Here, $\tilde{C}_p \equiv \langle \tilde{n}_p \tilde{n}_p^* \rangle$ represents the one-sided power spectrum, or the diagonal elements of the power spectral density matrix $\tilde{\boldsymbol{C}}$ for a total number of network devices N_d. There are several approximations we will make to simplify the likelihood in order to place order of magnitude estimates on the sensitivity. First, this assumes a network of identical uncorrelated devices that have a clock Allan deviation of $\sigma_y \equiv \sigma_y(T)$, with σ_y being the Allan deviation of the devices at sampling time T. Second, we assume that the signal is much smaller than the noise of the datastream at the limit of the device's sensitivity to the signal (i.e. $|s_{a,j}| \ll \sigma_y$). Third, we will assume we can approximate χ_p^2 with its ensemble average, that is the average of χ_p^2 over a large set of detector noise realizations. The ensemble average of χ_p^2 is expressed as

$$\langle \chi_p^2 \rangle = 2\sum_{a}^{N_d} \left(\left\langle \left|\tilde{d}_{a,p}\right|^2 \right\rangle + |\tilde{s}_{a,p}|^2 - \left\langle \tilde{d}_{a,p} \right\rangle (\tilde{s}_{a,p})^* - \left\langle \tilde{d}_{a,p} \right\rangle^* \tilde{s}_{a,p} \right) \Big/ \tilde{C}_p\ . \tag{3.31}$$

Since we assume white noise, $\tilde{C}_p = N\sigma_y^2$. Within the above formula, we can recognize the definition of the excess power statistic:

$$\varepsilon_p^a = 2\frac{|\tilde{d}_{a,p}|^2}{\tilde{C}_p} \; . \tag{3.32}$$

By construction, $\langle d_{a,p} \rangle = \langle d_{a,p} \rangle^* = 0$, and $\langle |d_{a,p}|^2 \rangle = N\sigma_y^2$, so the ensemble average of the excess power is $\langle \varepsilon_{a,p} \rangle = 2$. It can be shown that the Fourier power of the signal (if it is coherent sine wave of frequency f_p) with linear wave amplitude B is $|\tilde{s}_{a,p}|^2 \approx (NB/2)^2$. This is for a case where the Gaussian shape of the signal can be approximated by a step function of width τ. Using this, $\langle \chi_p^2 \rangle$ is:

$$\langle \chi_p^2 \rangle = 2\sum_w^{N_w}\sum_a^{N_d}\left(1 + \frac{|\tilde{s}_{a,w}|^2}{N\sigma_y^2}\right) \sim \frac{N_w N_d N}{2\sigma_y^2}\left(B^2 + \frac{2\sigma_y^2}{N}\right) , \tag{3.33}$$

From Bayes theorem, we know that the posterior distribution on the wave amplitude B is proportional to this likelihood. In the case of a uniform prior, we can compare the likelihood to a general posterior distribution on the wave amplitude B, where

$$\chi^2 = \left(\frac{B}{\sigma_B}\right)^2 \; . \tag{3.34}$$

We can then recognize that

$$\sigma_B \sim \sqrt{\frac{2}{N N_d N_w}}\sigma_y \; . \tag{3.35}$$

We will also assume we take statistically significant time windows (i.e. windows that do not overlap) so that the number of time windows is

$$N_w = \frac{\tau}{NT} \; , \tag{3.36}$$

for a signal duration τ and device sampling interval T. The noise floor for a network of precision measurement devices is then

$$\sigma_y \sqrt{\frac{2T}{\tau N_d}} \,. \tag{3.37}$$

3.3.3 Astrophysical reach of clock networks

Linear Coupling

An exotic scalar field ϕ can couple to atomic clocks based on linear scalar portals to standard model particles

$$-\mathcal{L}_{\text{int}} = \left[\sum_f \gamma_f m_f c^2 \bar{\psi}_f \psi_f + \frac{\gamma_\alpha}{4} F_{\mu\nu}^2 \right] \sqrt{\hbar c}\, \phi \,, \tag{3.38}$$

where m_f (ψ_f) are the fermion masses (fields) and $F_{\mu\nu}$ is the Faraday tensor, with γ_X being the associated coupling constants, where X runs over the fundamental constants (α, m_e, m_q), with α being the fine-structure constant and the m_e ans m_q are the electron and quark masses. In this framework, the combination of $\sqrt{\hbar c}\,\phi$ is measured in units of energy ($[E]$), while the γ_X are measured in $[E]^{-1}$. The coupling constants can also be defined in terms of the effective energy scale $\Lambda_X = 1/|\gamma_X|$. These interactions lead to the effective redefinition of fermion masses and constants,

$$\begin{aligned} m_f^{\text{eff}} &= m_f \Big(1 + \sqrt{\hbar c}\ \gamma_f \phi \Big) \,, \\ \alpha^{\text{eff}} &= \frac{\alpha}{\Big(1 - \sqrt{\hbar c}\, \gamma_\alpha \phi \Big)} \approx \alpha \Big(1 + \sqrt{\hbar c}\, \gamma_\alpha \phi \Big) \,. \end{aligned} \tag{3.39}$$

With this effective change in fundamental constants, the fractional frequency shift in the clock frequency ν_a can be expressed as

$$\frac{\delta\nu_a}{\nu_a} = \sqrt{\hbar c}\,\sum_X \kappa_X \gamma_X \phi = \Gamma_{\text{eff}}\phi, \tag{3.40}$$

where κ_X are the sensitivity coefficients, and Γ_{eff} is the effective field coupling constant to the clocks. This fractional frequency shift can be related directly back to our data in Eq. 3.29. For the purpose of estimating the GPS network sensitivity to ELFs, we assume the coupling to α dominates (i.e., $\Gamma_{\text{eff}} \approx \sqrt{\hbar c}\,\kappa_\alpha \gamma_\alpha$).

From Eq. (3.7), we know the ELF amplitude to be

$$A \approx \frac{1}{\omega_0}\sqrt{\frac{c\Delta E}{2\pi\tau}} = B_1 r\ . \tag{3.41}$$

The fractional frequency shift of the clock frequency ν_a, if we assume the coupling to α dominates, is

$$\frac{\delta\nu_a}{\nu_a} = \Gamma_{\text{eff}}\phi \sim \kappa_\alpha \Gamma_\alpha \phi\,. \tag{3.42}$$

The definition of the electromagnetic gauge modulus d_e relative to the coupling constant Γ_α is

$$\Gamma_\alpha = \left(\frac{\sqrt{4\pi G}}{c^2}\right) d_e\,. \tag{3.43}$$

Plugging in $\phi = B_1$, we can then form the signal to noise ratio

$$\text{SNR} = \frac{\kappa_\alpha d_e}{\omega_0 r}\sqrt{\frac{2G\Delta E}{c^3\tau}} \Bigg/ \sigma_y \sqrt{\frac{2T}{\tau N_d}}\,. \tag{3.44}$$

Requiring an SNR ~ 1 leads to an expression for the smallest detectable value of the electromagnetic gauge modulus d_e with a fixed observation distance R:

$$|d_e| < \frac{\omega_0 \sigma_y(T) R}{\kappa_\alpha} \sqrt{\frac{c^3 T}{G \Delta E N_d}} \,. \tag{3.45}$$

If instead we pick $|d_e|$ fixed by equivalence principle constraints [62], this can be rearranged into the maximum discovery reach:

$$r \sim \frac{\kappa_\alpha |d_e|_{\mathrm{EPV}}}{\omega_0 \sigma_y(T)} \sqrt{\frac{G \Delta E N_d}{c^3 T}}, \tag{3.46}$$

Using the definition of the electromagnetic gauge modulus $d_e = (E_p/\sqrt{4\pi})\gamma_\alpha$ [62] where the Planck energy $E_p = \sqrt{\hbar c^5/G}$, we can obtain an expression for the coupling constraints,

$$|d_e| < \frac{\omega_0 \sigma_y(T) R}{\kappa_\alpha} \sqrt{\frac{c^3 T}{G \Delta E N_d}} \,. \tag{3.47}$$

where G is the gravitational constant, $\sigma_y(T)$ is the Allan deviation of the clocks, T is the sampling interval of the clocks, and N is the number of clocks in the network. If we use the equivalence principle violation constraints $d_e < 10^{-3}$ [62], we can solve for the maximum discovery reach. We use $T = 1$s throughout our analysis as it gives us the highest currently achievable frequency range with the GPS network. If we pick optimal values for the parameters in Eq. (3.47), this can function as a maximum sensitivity for the clock networks. For Rb clocks, the sensitivity coefficient is $\kappa_\alpha = 2$, and they have a typical Allan deviation $\sigma_y(1\mathrm{s}) \approx 10^{-13}$. This leads to an astrophysical range of $\approx 10^4$ ly for a detector network of 100 conventional devices, which is achievable with the incorporation of other satellite positioning networks such as the European Galileo constellation. Laboratory clocks based on Yb atoms have much better Allan deviation ($\sigma_y(1\mathrm{s}) \approx 10^{-16}$ [63, 64]) and can reach farther at $\approx 10^5$ ly, encompassing the whole of the Milky Way. Potential future Th based nuclear clocks have a much higher projected sensitivity coefficient $\kappa_\alpha \approx 10^5$ [65], and an Allan deviation $\sigma_y(1\text{s}) \approx 10^{-14}$ [66]. This will allow for a maximum range of $\approx 10^8$ ly, which is enough range to search for ELFs near the time of the known neutron star merger event GW170817. These estimates are reflected in Table 3.2a.

Quadratic Coupling

For the case of quadratic coupling to ELFs, the interaction can be written as:

$$-\mathcal{L}_{\text{int}} = \left(\sum_f \frac{m_f c^2 \bar{\psi}_f \psi_f}{\Lambda_f^2} - \frac{1}{4\Lambda_\alpha^2} F_{\mu\nu} F^{\mu\nu} \right) \hbar c\, \phi^2 \,, \tag{3.48}$$

where instead of coupling constants used before, we have parameterized the interaction in terms of the effective energy scales Λ_X. This interaction leads to effective redefinition of fundamental constants similar to the linear coupling,

$$\begin{aligned} m_f^{\text{eff}} &= m_f \left(1 + \hbar c\, \frac{\phi^2}{\Lambda_f^2} \right), \\ \alpha^{\text{eff}} &= \frac{\alpha}{(1 - \hbar c\, \phi^2/\Lambda_\alpha^2)} \approx \alpha \left(1 + \hbar c\, \frac{\phi^2}{\Lambda_\alpha^2} \right), \end{aligned} \tag{3.49}$$

which leads to the fractional frequency shift of the unperturbed clock frequency ν_{clock},

$$\frac{\delta \nu_a}{\nu_a} = \hbar c \sum_X \kappa_X \frac{\phi^2}{\Lambda_X^2} \equiv \hbar c\, \frac{\phi^2}{\Lambda_{\text{eff}}^2}, \tag{3.50}$$

The main difference from the previous case is that the field model is squared in the interaction. Using the power reduction formula for cosine wave, the squared model yields two terms,

$$\phi(r,t)^2 \approx \frac{A_0^2}{r^2} \frac{\tau_0}{2\tau} \exp\left(-\frac{(t-t_s)^2}{\tau^2} \right) \left[1 + \cos\left(2\omega_0 (t - t_s) - \frac{1}{\tau_0 \tau} (t - t_s)^2 \right) \right] . \tag{3.51}$$

The first term is just a Gaussian, while the second term is an oscillation with Gaussian amplitude. The frequency of the oscillation is easily comparable to the linear model, as the central frequency and the slope are effectively doubled in the signal.

The statistics from the linear coupling section will remain the same, but the effective quadratic signal amplitude B_2 will be different,

$$\frac{\hbar c\, A^2}{2r^2} \approx \frac{\hbar c^2}{2r^2\omega_0^2}\frac{\Delta E}{2\pi\tau} \equiv B_2 \ . \tag{3.52}$$

Assuming again that the coupling to α dominates, we can form the SNR for $\phi^2 = B_2$:

$$\mathrm{SNR} = \frac{\hbar c^2}{4\pi}\frac{\kappa_\alpha}{\Lambda_\alpha^2}\frac{\Delta E}{\omega_0^2 r^2\tau} \Bigg/ \sigma_y\sqrt{\frac{2T}{\tau N_d}} \ . \tag{3.53}$$

Requiring an SNR ~ 1 and using Eq. 3.15 to substitute for τ, leads to an expression for the largest effective energy scale for the quadratic interaction:

$$\Lambda_\alpha^2 > \frac{\hbar^2}{2m}\frac{\kappa_\alpha \Delta E}{2\pi\sigma_y}\sqrt{\frac{cN_d\tau_0}{2T\omega_0 r^5}} \ . \tag{3.54}$$

If instead we pick Λ_α fixed by astrophysical constraints [67], this can be rearranged into the maximum discovery reach:

$$r^{5/2} \sim \frac{\hbar^2}{2m}\frac{\kappa_\alpha \Delta E}{2\pi\sigma_y(\Lambda_\alpha)^2_{\mathrm{AC}}}\sqrt{\frac{cN_d\tau_0}{2T\omega_0}} \ . \tag{3.55}$$

If we compare the maximum Λ_α which we are sensitive to the astrophysical constraints $\Lambda_\alpha > 10\,\mathrm{TeV}$ [67], we can see the amount of parameter space we are able to explore. The sensitivity coefficients and Allan deviation for the clock types we consider are the same as in the linear coupling. For the case of Thorium clocks, the maximum Λ_α is five orders of magnitude above current constraints. This is outlined in Table 3.2b.

3.3.4 ELF event rates

The starting point for estimating the ELF burst rate is to determine the number of relevant astrophysical events in a given cosmic volume. In our case, we include binary black hole mergers, binary neutron star mergers, and mergers of black hole with a neutron star, although ELF bursts may also come from other sources. Recent studies [17, 68–72] based on observed gravitational wave events estimate the binary merger rates may be as large as $\gamma(\mathrm{BH}-\mathrm{BH}) \sim 200\ \mathrm{Gpc}^{-3}\mathrm{yr}^{-1}$, $\gamma(\mathrm{NS}-\mathrm{BH}) \sim 3000\ \mathrm{Gpc}^{-3}\mathrm{yr}^{-1}$, and $\gamma(\mathrm{NS}-\mathrm{NS}) \sim 5000\ \mathrm{Gpc}^{-3}\mathrm{yr}^{-1}$. We conclude that it is reasonable to assume a generic binary merger rate of $\gamma \sim 10^3\ \mathrm{Gpc}^{-3}\mathrm{yr}^{-1}$.

A cosmic volume of 1 Gpc^3 contains roughly 10^9 galaxies, so based on the above estimate for γ, the rate of binary mergers in the Milky Way is $\sim 10^{-6}\ \mathrm{yr}^{-1}$. Increasing the sensitivity of the clocks has a dramatic impact on detectable events: the cosmic volume probed is proportional to the cube of the sensor sensitivity.

Binary merger event rates within the Milky Way are $\ll 1/\mathrm{yr}$ for the linear coupling, but the quadratic coupling shows much higher sensitivity to ELFs. Future technologies will also offer the possibility of much greater sensitivity and therefore greater astrophysical reach (Table 3.2).

(A) ELF Sensitivity for Linear Coupling

Clock Network	Allan deviation $\sigma_y(1\text{s})$	Astrophysical reach (ly)	Detection rate (1/yr)
GPS	10^{-13}	10^3	-
Optical lattice clocks ($\star$)	10^{-16}	10^5	10^{-6}
Th nuclear clocks ($\star\star$)	10^{-14}	10^8	1

(B) ELF Sensitivity for Quadratic Coupling

Clock Network	Allan deviation $\sigma_y(1\text{s})$	Highest Sensitive Coupling (TeV)
GPS	10^{-13}	10^3
Optical lattice clocks ($\star$)	10^{-16}	10^5
Th nuclear clocks ($\star\star$)	10^{-14}	10^6

Table 3.2: Estimated sensitivity to ELFs, astrophysical reach, and event rates for existing, planned ($\star$), and possible ($\star\star$) sensor networks, where the event rates assume an ELF energy release of $\Delta E \approx M_\odot c^2$ and a generic binary merger rate density of 10^3 Gpc^{-3}yr^{-1}. Table (A) uses electromagnetic gauge modulus set by equivalence principle constraints $d_e \approx 10^{-3}$. Table (B) gives maximum effective energy scale that we are sensitive to, which is to be compared to the current astrophysical limits $\Lambda_\alpha \approx 10$ TeV.

Chapter 4

Search Results

4.1 Introduction

After the discovery of a multi-messenger signal from a neutron star merger (NSM) announced by the LIGO team in 2017 [10], there was growing interest in the GPS.DM group to search for a signal that could be correlated to NSM events. Other gravitational wave events, like black hole mergers, can also be of interest, but all of the black hole events announced prior to this work do not have a well characterized source direction, as they are not expected to have an electromagnetic counterpart. In contrast, the GW170817 NSM is known to have a source in the galaxy NGC 4993 and had a coalescence time of 2017-08-17 12:41:04 UTC, allowing for an easily falsifiable effect if one exists [10]. For this reason, this event was chosen to carry out the first proof-of-principle search for ELFs using the GPS.DM Observatory. One detail that is important to consider is that the GPS time-series data is normally sampled with a 30 second interval, but this rate does not give much time or frequency resolution for analysis, since the NSM lasted less than 1 minute in LIGO's sensitivity range. As mentioned before however, our group has shown that it is possible to generate GPS clock data with a 1 s sampling interval, which we used to carry out this first proof-of-principle search.

The goal of this search was to investigate the time-frequency space of each satellite's clock time-series data in an attempt to find any anomalous features that may be correlated to the gravitational wave event GW170817. In particular, we are interested in signals that may be described by the ELF dispersion model [Eq. (3.17)]. This is similar to how the LIGO collaboration represents and searches with pattern matching techniques for their gravitational wave signals.

The first set of data produced was generated by Geoff Blewitt in the GPS.DM collaboration in 2018 using the then recently released GipsyX software. Once this data was analyzed, it became clear that these data were filled with oscillating signals with time-varying frequencies for many of the clocks in the network. Several alterations to the data were attempted in order to discern the potential cause of the signals, such as changing the reference clock. The signals seemed to disappear or change when the reference clock was switched, which is why we began using the data pre-processing method outlined in Section 3.3.1 to help remove the reference clock contributions. After further investigation, some interesting signals remained unexplained, and it soon became clear that the GPS.DM sourced data would not be sufficient to discern the cause of these remaining signals. The analysis for this data is outlined in detail in Section 4.3. After this the GPS.DM collaboration requested JPL to generate 1 s data directly.

Correspondence with JPL lead to more optimal datasets being generated, which helped answer some remaining questions about the signals. The data spanned a time period of 30 hours, 10 times longer than the previous dataset. We found that the signals were not just an artifact of the GPS.DM data generation, and they seemed to repeat at a nearly daily rate for a given satellite time-series. The analysis for the JPL sourced data is discussed in detail in Section 4.4. Due to many satellites having unique daily repeating signals, we chose to analyze a weighted network average time-series to investigate possible signals that would affect every clock in the network. No obvious signals were found and we left limits to be derived by future work.

4.2 Data Processing

To determine if clocks in the GPS.DM network detected any ELF signals, we use an excess power statistic , which is defined in detail in [73]. This method is based on the time-frequency decomposition of the dataset, and highlights frequency excursion events based on the signal power in a time-frequency interval compared to the detector noise. Excess power is the optimal method for searching for events in situations for which only a rough idea of the frequency and duration of the signal is known [73, 74], but can be generalized to include a specified signal such as the ELF model in Section 3.2.3.

If we use some generic sampling rate $1/T$ for the clocks and apply our pre-processing method from Section 3.3.1, we get a resulting pseudo-frequency time-series from a clock denoted $d_{a,j}$. Following the treatment in Ref. [73], we consider each point as comprising contributions from both a potential signal $s_{a,j}$ and the detector noise $n_{a,j}$,

$$d_{a,j} = s_{a,j} + n_{a,j}\,. \tag{4.1}$$

We partition the data into segments of discrete time and frequency "tiles". Our goal is to quantify the power contained in each segment of the data due to only noise, and due to possible contributions from ELF signals. We assume that measurements made before the electromagnetic or GW signal associated with the astrophysical event were detected on Earth have vanishing ELF signal content and that data taken after the EM detections may contain ELF signals. We define a time width for each tile, $\delta\tau = NT$ and parse the data from each clock into segments of length N. The center of each segment is then interpreted as the time of occurrence of the frequency tiles. It should be noted that N is chosen to be an even number to ensure that there is a well-defined Nyquist frequency, so there is no epoch directly in the center of this window. The center time is then the time directly between the two middle epochs, and we choose an epoch index w that represents the epoch immediately following the time in the center of the segment. This means that the center time of the sub-window is a half epoch behind the time that $d_{a,w}$ was sampled. The Fourier transform of the data in this window for the k^{th} frequency index is defined as [20]:

$$\tilde{d}_{a,k} = \sum_{j=0}^{N-1} d_{a,j} e^{2\pi ijk/N} \,. \tag{4.2}$$

The frequency index k here goes from 0 to the Nyquist frequency $1/(2T)$. For every a^{th} clock and window off-center epoch w there is $N/2+1$ unique frequencies in this transform. It should be noted that the total time window in Fourier space is decreased by N epochs because both the beginning and end of the window can only fit a sub-window with a center epoch at $N/2$ epochs away from the end of the time-series data. We define the excess power in each time-frequency tile as

$$\varepsilon_{a,k,w} = 2\frac{|\tilde{d}_{a,k,w}|^2}{\tilde{C}_{a,k}} \,, \tag{4.3}$$

where $\tilde{C}_{a,k}$ is the one-sided power spectrum of the noise of each clock via $\tilde{C}_{a,k} = \langle \tilde{n}_{a,k}\tilde{n}^*_{a,k}\rangle$. Dividing the data power in each tile by $\tilde{C}_{a,k}$ effectively normalizes the power spectrum, so that each frequency component of the statistic has the same expectation value.

For detectors characterized by stationary Gaussian noise, the excess power $\varepsilon_{a,k,w}$ is a random variable drawn from a chi-squared distribution with probability density function

$$f_{\chi^2}(\varepsilon, V) = \frac{\varepsilon^{V/2-1}e^{-\varepsilon/2}}{2^{V/2}\Gamma(V/2)} \,, \tag{4.4}$$

which has $V = 2\delta f \delta t$ degrees of freedom [73]. The excess power in tiles containing an actual signal will be larger than expected; signal containing tiles will consequently be located in the tail of an excess power histogram.

```
FILE:        ../unr19621.clk_1s
DATA START: 2017  8  14 11  0  0 0.000000000
DATA END:   2017  8  14 14 14 59 0.000000000
UTC = GPSEC -18
REFCLOCK:   AMC2
T CLOCK  WEEK  D  GPSEC          BIAS(s)            ERROR(s)
S  GP59  1962  1  39600  -4.911305419743e-04  4.202907599497e-11
S  GP53  1962  1  39600  -1.635361653119e-04  4.139530421409e-11
S  GP56  1962  1  39600   3.669877308173e-05  3.712568379555e-11
S  GP51  1962  1  39600   4.832108737862e-04  3.695890174796e-11
S  GP45  1962  1  39600  -4.872613870568e-04  3.475737871965e-11
S  GP73  1962  1  39600   3.678649477822e-05  3.635848637660e-11
S  GP71  1962  1  39600  -4.523770397858e-04  3.805966326211e-11
S  GP70  1962  1  39600  -4.827609710375e-04  5.180250398427e-11
S  GP62  1962  1  39600  -4.388287254545e-04  4.456416311847e-11
S  GP58  1962  1  39600   3.760373102014e-04  4.212914522353e-11
S  GP57  1962  1  39600   5.747527332699e-04  3.789288121451e-11
S  GP54  1962  1  39600   6.269602872611e-04  3.715904020507e-11
S  GP52  1962  1  39600   1.819683822863e-04  4.549814258503e-11
S  GP41  1962  1  39600  -8.077414656965e-05  5.313676036507e-11
S  GP67  1962  1  39600   3.880810632997e-04  4.696582460390e-11
S  GP65  1962  1  39600  -3.883287899009e-05  3.705897097651e-11
S  GP61  1962  1  39600   3.543826175994e-04  3.622506073852e-11
S  GP55  1962  1  39600  -3.546627798434e-04  3.445717103397e-11
S  GP43  1962  1  39600  -8.958050890207e-05  3.345647874837e-11
S  GP72  1962  1  39600  -6.984173842478e-05  3.220561339138e-11
S  GP66  1962  1  39600   3.101241527767e-04  3.243910825802e-11
S  GP64  1962  1  39600   1.458369975513e-04  3.277600799417e-11
S  GP60  1962  1  39600  -2.162819119537e-04  4.473094516607e-11
S  GP50  1962  1  39600  -3.329427130485e-05  3.425703257685e-11
S  GP48  1962  1  39600   3.157745724717e-04  3.465730949109e-11
S  GP44  1962  1  39600   6.372499732393e-04  3.318295619031e-11
S  GP36  1962  1  39600   9.821802166687e-06  3.765938634787e-11
R  TOW2  1962  1  39600   5.443978278731e-09  3.352319156741e-11
R  THTI  1962  1  39600  -3.322051427275e-08  3.605827869092e-11
R  RABT  1962  1  39600  -5.387211801290e-08  2.993404190308e-11
R  POL2  1962  1  39600  -6.061515342603e-08  3.113820828675e-11
R  PIMO  1962  1  39600  -5.559395155932e-09  3.324633336840e-11
R  PDEL  1962  1  39600  -2.433075424754e-09  3.098143316200e-11
```

FIGURE 4.1: Small section of the GPS.DM sourced 1 s interval file structure. The first row is the file name, the second row is the UTC time of the first epoch of data given, the third is the UTC time of the last epoch of data given, the fourth row gives the time difference between GPS time and UTC time in seconds (due to leap seconds), and the fifth row gives the name of the reference clock. The next rows are column titles and then the data stream. The first column specifies satellite or earth-based clocks, the second gives the clock name (SVN for satellites), then the week number, the day number, the epoch of the day, the clock bias value, and finally the formal error.

4.2.1 File Structure Conversion

There are several details to keep in mind before we can begin the analysis. What we desire is a table of values where each clock is a row and each epoch is a column, but the JPL files were sorted by epoch number (see Figure 4.1), that is to say that for each data sample, there is a table of values for every clock. There may also be missing data points for certain clocks at each epoch.

To mitigate these problems, for every missing data point, a new row is created and zero is written as a placeholder in the bias column. For now, we don't include analyses for any clocks that have zeros anywhere in the window after this processing. We also make sure that all of the clocks that we analyze are common to all of the files, dropping any that are do not appear in every dataset. Now that the file has a predicable length due to this buffering, we keep only the clock name, epoch number, and bias value as information and sort it into a table of values where the rows are the epoch numbers and the columns are the specific clocks, with each element being the bias for each clock and epoch.

4.3 Results from GPS.DM Sourced Data

Our first attempt to analyze GPS clock frequency data started with the production of 1 Hz sample rate GPS time-series data with the GipsyX software package. Five files were generated, each spanning 3 hours, and each file starting at 11:00 UTC spanning the dates 2017-08-14 to 2017-08-18 (GPS days 19621-19625). The fourth file in the list corresponds to the GW170817 event which has a UTC merger time of 2017-08-17 12:41:04 UTC. The purpose of the files on different days other than the NSM event is get a good average of the power spectral density of the clocks and to compare the files for similarities. For this initial attempt, it was only possible to generate files of ~ 3 hour duration for a total of 31 satellites. Here, we only analyzed data from satellite clocks due to many of the earth-based station clocks not being well-behaved in frequency space. Many of the Earth-based clocks have unique trends and perturbations that do not correlate with other clocks (example shown in Figure 4.2 in contarst to Figure 4.3). Some even have noise profiles that are clearly not white, even after differencing. For this reason, we do not include them in the analysis.

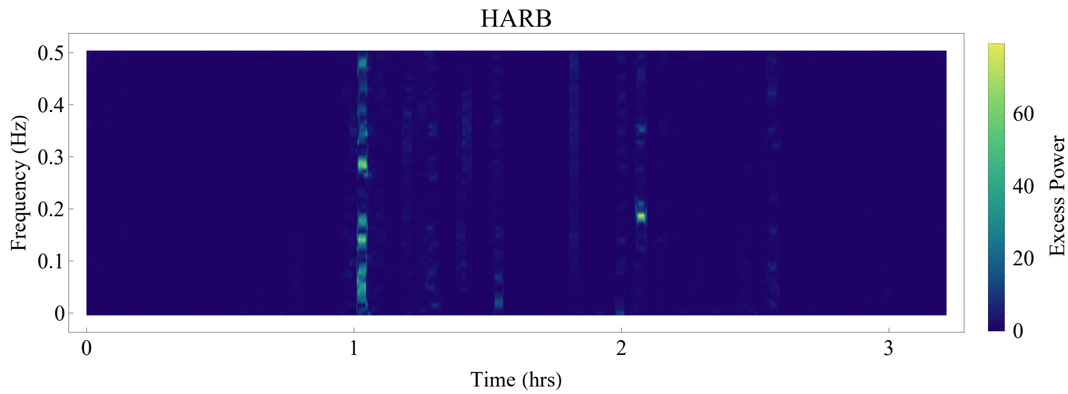

FIGURE 4.2: Example of a badly-behaved Earth-based clock (identifier HARB). There are many perturbations across all frequencies in the middle of the window that are so large that the noise of the clock is lost in the plot. The maximum normalized power is also very high compared to the well-behaved clock. These perturbations are unique to this clock, and very likely a glitch in this specific time-series.

As discussed before, our data analysis method produces a "power chart" that represents the time-frequency space of a specific satellite clock's pseudo-frequency. We have left out clocks that have missing data points within any of these datasets, which leaves 20 satellite clocks.

Several of these charts have interesting signals within them. Figure 4.4 depicts a satellite with identifier GP55. There is a linearly decreasing signal that repeats each day, with a repetition time near that of the orbital period of the satellite. What is curious about this is that the formal error that describes how well the solution was fit also repeats near this rate. This is likely to do with the satellite moving over different parts of the Earth, where there may be more or less stations visible.

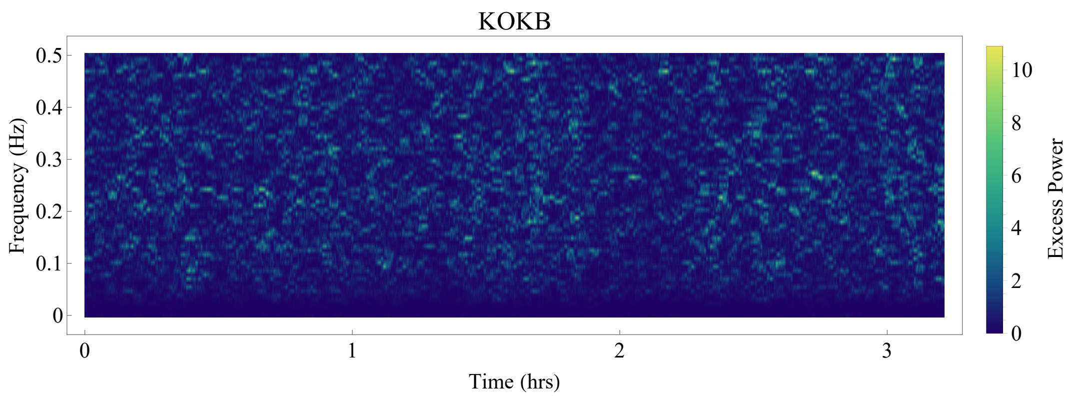

FIGURE 4.3: Example of a Earth-based clock with non-white noise (identifier KOKB). The the noise seems to get quieter as the frequency is decreased, however there are no obvious glitches or easily identified perturbations in the spectrum.

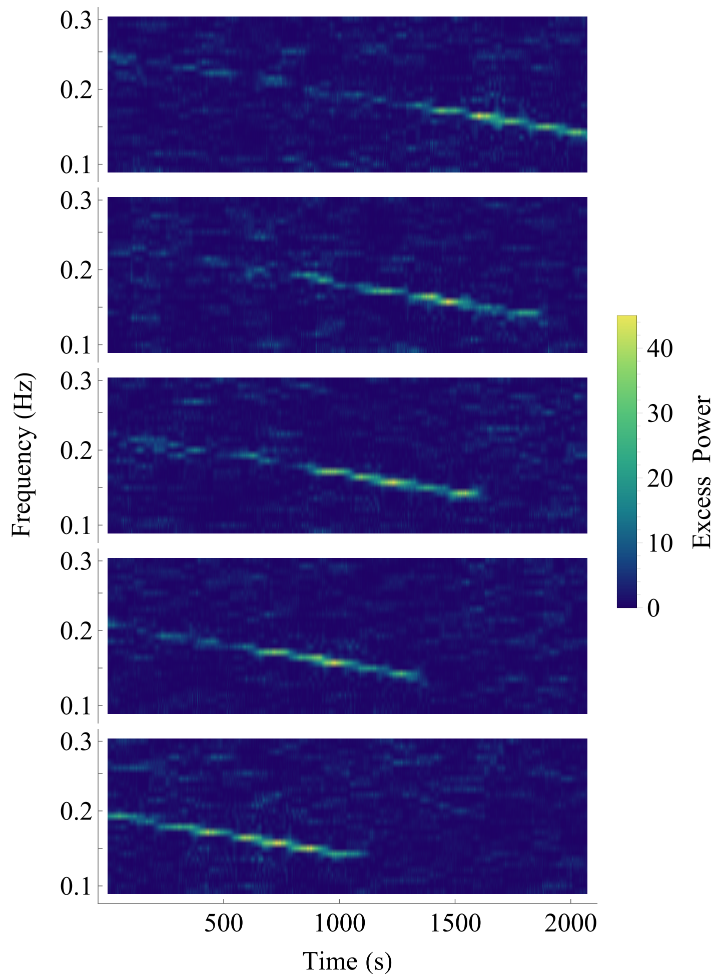

Figure 4.4: Five plots that represent a sample of the time frequency space taken from one satellite with identifier GPS55. There is exactly 24 hours of time in between the start of each plot, with a common start time of 1:38:20 UTC. There is a repeating decreasing frequency signal, that builds in amplitude before maximizing at about 0.15 Hz. The time difference between each successive amplitude maximum of the signal is about 250 seconds less than 24 hours, which is close to twice the orbital period of this satellite.

The search for ELFs in this case is severely limited as there is only a small amount of time immediately following the merger event in order to constrain the velocity of the field. This also limits the maximum temporal duration of the wavepacket that we can observe. Despite this, our search found interesting frequency excursion signals. Some of these signals appear to match what might be expected from the ELF dispersion model from Fig. 3.2. As a first sanity check we looked at the data generated on the days before and after the GW170817 event. We found that many of these signals seemed to repeat on a cycle with period near that of a sidereal day. An example of this can be found in Figure 4.4. Physical intuition about the GPS constellation led us to suspect that the signals might repeat at a period matching that of the satellite orbital period of about half a sidereal day. It might also cycle at the period of terrestrial position repetition, which is 2 orbital periods, or near 1 sidereal day. Due to the limited amount of data we generated on this first attempt, we could not discern if the signals repeated at a rate faster than a sidereal day or at a sidereal day. This spurred our collaboration with JPL, where we requested 1 Hz data files with full 30 hour duration.

4.4 JPL Sourced Data

With the goal of distinguishing the repetition time of the frequency excursion events outlined in the previous section and to make sure the data was reproducible, we collaborated with JPL to produce 1 s data for longer stretches of time. We found that the data was in agreement to the previously generated data.

We received two separate datasets from JPL, each spanning 30 hours. Each file completely spans one day, with a start time of 21:00 UTC the previous day and and end time of 3:00 UTC the following day. We requested the dates 2017-08-17 and 2017-08-16 so that we would have enough time span to discern the signal repeat rate mentioned above. These first datasets used reference clock AMC2, but we found that this reference clock was badly behaved during this time period. We then requested new datasets be generated with reference clock BRUX, which we found to be much better behaved. This is demonstrated by Fig. 4.5.

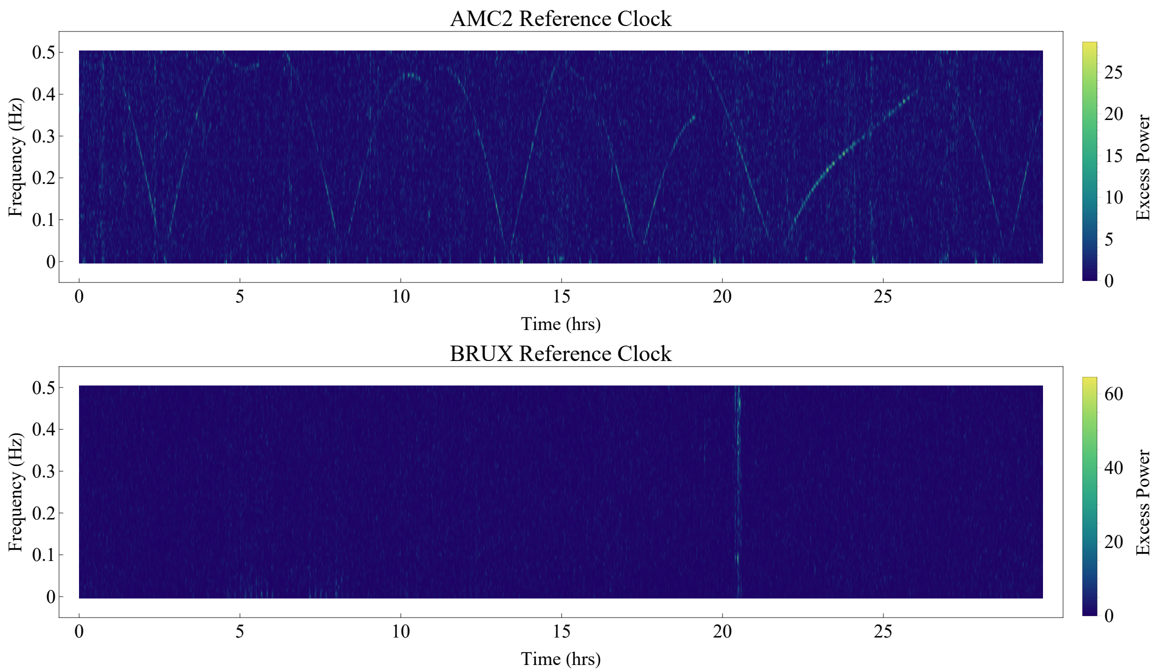

FIGURE 4.5: Representation of the AMC2 and BRUX reference clocks in time-frequency space. These plots, both spanning the date 2017-08-17 and starting at 2017-08-16 21:00 UTC, are very different as the AMC2 reference clock contains many time-varying frequency signals. Changing the reference clock to BRUX removes all of the signals besides a glitch near the 20 hour mark, suggesting that AMC2 is badly behaved.

Every clock in these datasets seemed to have a unique repeating signal, which is in contrast to what would be expected for an ELF signal that affects all of the clocks at once. Fig. 4.6 shows an example of a repeating signal for satellite clock GPS58. The signal repeats near the a period of a sidereal day, which suggests that these signals have an origin that depends on what terrestrial stations are in view to the satellite, as this repeats with this period. The other analyzed satellite plots can be found in Appendix A.

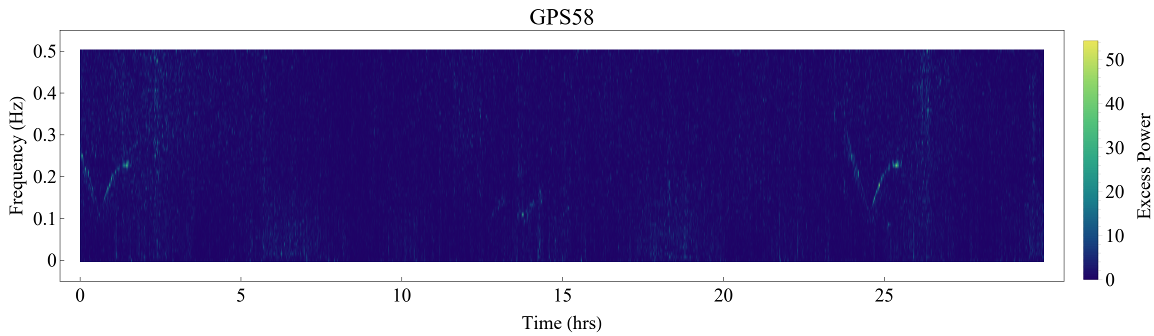

FIGURE 4.6: Emphasis of repeating signals in the satellite clock GPS58. The time-dependent frequency signals near the 0 hr and 25 hr marks have the same general form and repeat near 2 orbital periods of the satellite.

To ensure our analysis does not include these repeating signals, we then took a network average of the data. The ELF model we have outlined should affect every clock in the network in the same way and at the same time, so this average should make any common signals much more obvious. The network average plot is shown by Fig. 4.7. We found that this network average has a distribution of excess power values that matches the probability distribution one expects for Gaussian white noise, which is shown in Fig. 4.8.

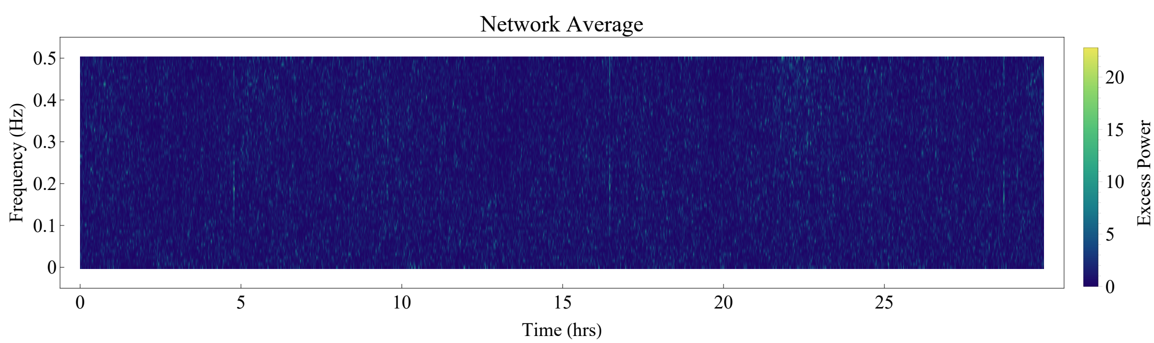

FIGURE 4.7: The network average plot. There does not appear to exist any obvious frequency excursion events consistent with the ELF model. There are some vertical lines here, near the 5 hr and after the 15 hr marks, but these signals correspond to data outliers.

Within the network average, we observed no statistically significant frequency excursion events consistent with the ELF model. This is shown by the excess power histogram Fig. 4.8

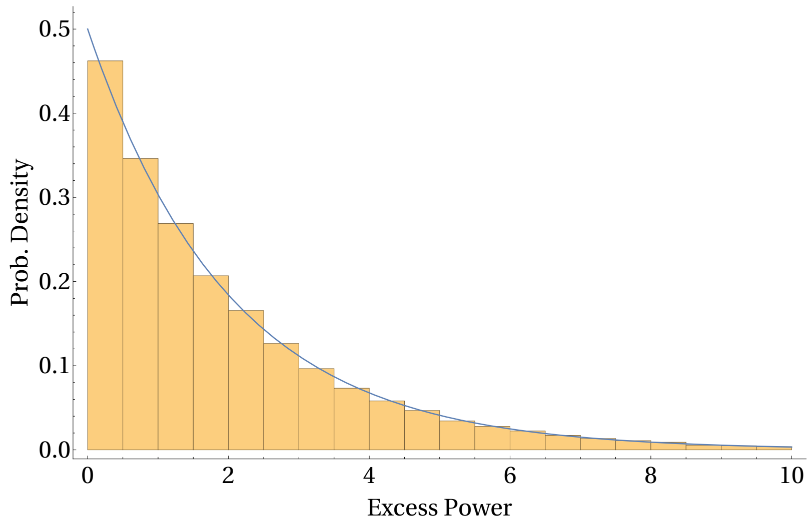

FIGURE 4.8: Histogram showing the comparison of excess power values in Fig. 4.7 to the expected probability density distribution. The distribution of excess power values matches white noise very well.

which is inconsistent with what would be expected by a signal-containing dataset. Rigorous statistical limits are left for future work, as longer stretches of data can set much more competitive limits and this 1 s data needs further characterization.

4.5 Future Work

The analysis performed in this work is purely a proof-of-principle, since much of it is based on 1 s sampling interval GPS data that is state-of-the-art. We focused on only one event in this work, but there does exist about 20 years of archived data that could be searched in a similar manner. In particular, known events such as gamma ray bursts, fast radio bursts, super novas, and solar flares could be correlated with the sought ELF events. One challenge to this is the repeating nature of the clock data signals found in the previous sections. One possibility to mitigate this is to remove auto-correlations at the repetition rate for each clock. This will allow us to search for signals that do not repeat at the rate we have identified. We can also mitigate the problem of of missing data points for some time-series by implementing a frequency analysis based on periodograms, which mimics a least squares fit to wave-forms instead of using the Fourier transform. With these future points, there is much left to explore using GPS.

Chapter 5

Conclusion

In this work we have demonstrated the ability of global networks of precision measurement devices to detect ELFs that may be emitted from high energy astrophysical events, potentially making them a new messenger in the growing field of multimessenger astronomy. We discussed using the atomic clocks that make up GPS as such a network, along with future networks of atomic clocks, and we characterized how ELFs may interact with them. We have developed a model for the time evolution of pulses of ultrarelativistic matter waves, and estimated the sensitivity of GPS and future networks of atomic clocks to detect ELFs. We have shown that quadratic couplings to ELFs have great potential for detection with GPS and that future networks of atomic clocks have even greater sensitivity. This work has also uncovered previously unknown time-frequency behavior of the GPS satellite clocks, as our analysis is the first to be preformed on high-rate GPS clock data. While we have shown that these time-frequency signals are not likely caused by ELFs, their origin still remains a mystery and certainly invokes questions about the behavior of the GPS network. A complete characterization of the clock behavior we have discovered could be used to improve the modeling and quality of GPS. The search for ELFs based on this event was limited in this case due to the limited data available, but this search can be extended to times much longer after the GW170817 event itself to consider ELFs of slower (though still ultra-relativistic) velocities. Future work in the search for ELFs can include analysis at known times of past astrophysical events, such as gamma ray bursts, black hole mergers, and solar flares.

Appendix A

JPL Sourced Data Plots

This section presents time-frequency plots of the excess power for each satellite with a complete dataset. The start of each file is 2017-08-16 21:00 UTC and it ends at 2017-08-18 3:00 UTC.

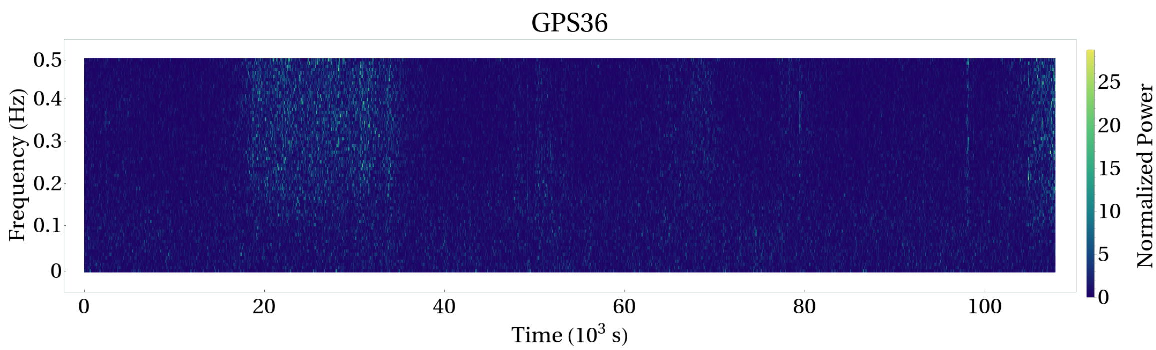

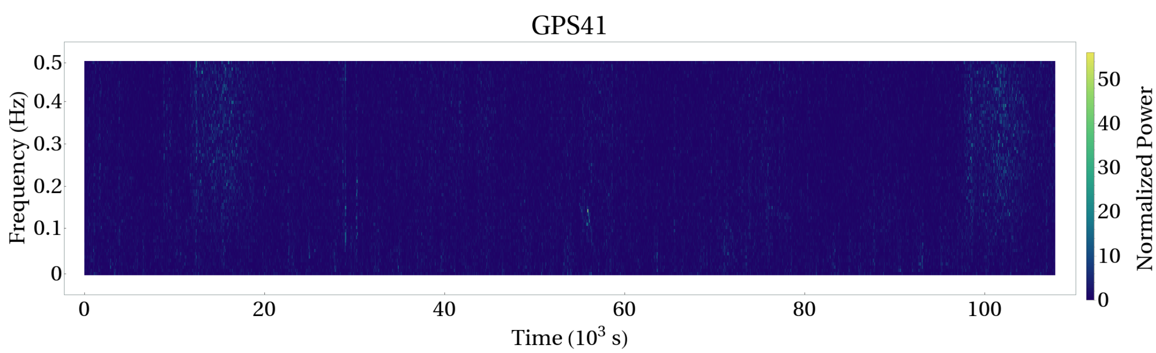

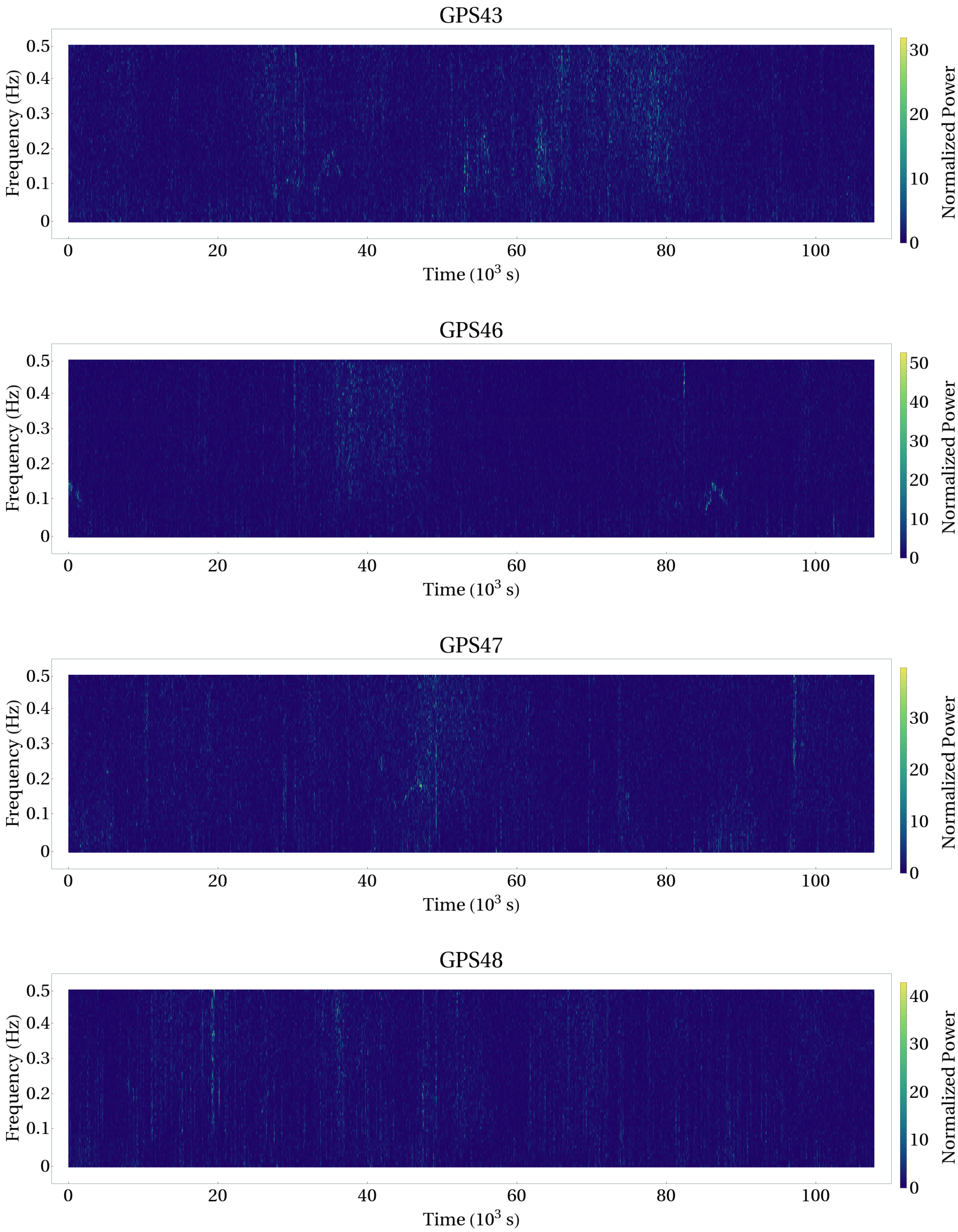
GPS43
GPS46
GPS47
GPS48
Frequency (Hz)
Time (10^3 s)
Normalized Power
0
0.1
0.2
0.3
0.4
0.5
20
40
60
80
100
10
30
50

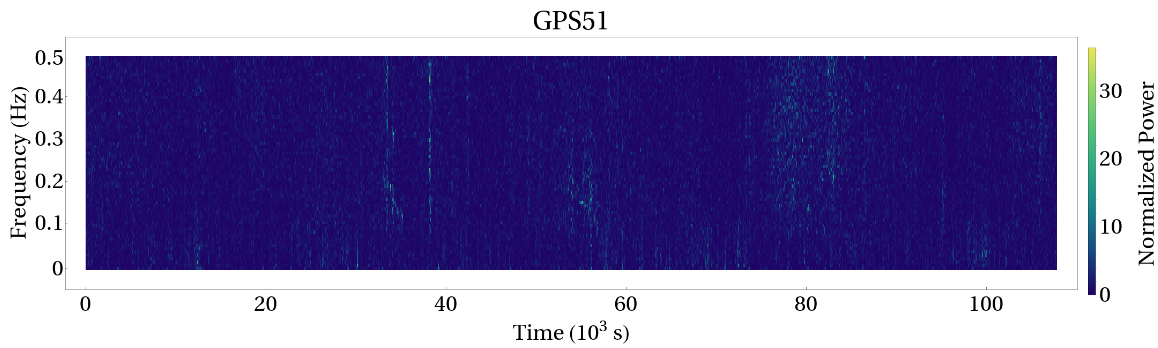
GPS51
Frequency (Hz)
Time (10^3 s)
Normalized Power
0 0.1 0.2 0.3 0.4 0.5
0 20 40 60 80 100
0 10 20 30

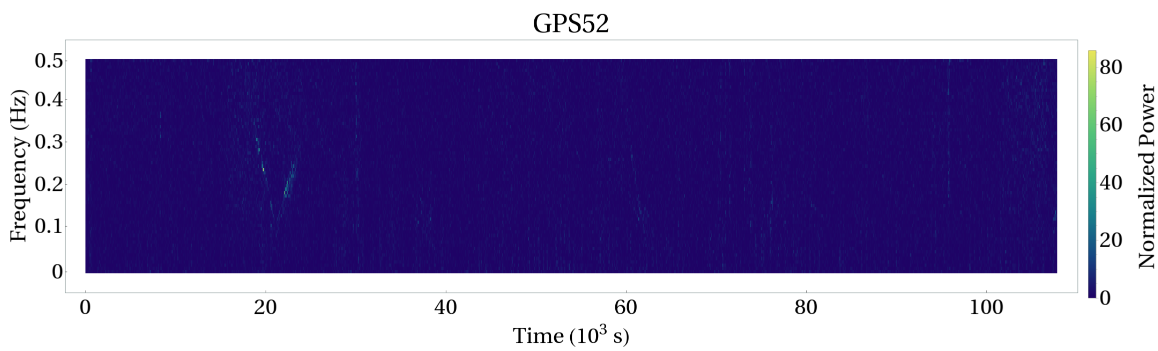
GPS52
Frequency (Hz)
Time (10^3 s)
Normalized Power
0 0.1 0.2 0.3 0.4 0.5
0 20 40 60 80 100
0 20 40 60 80

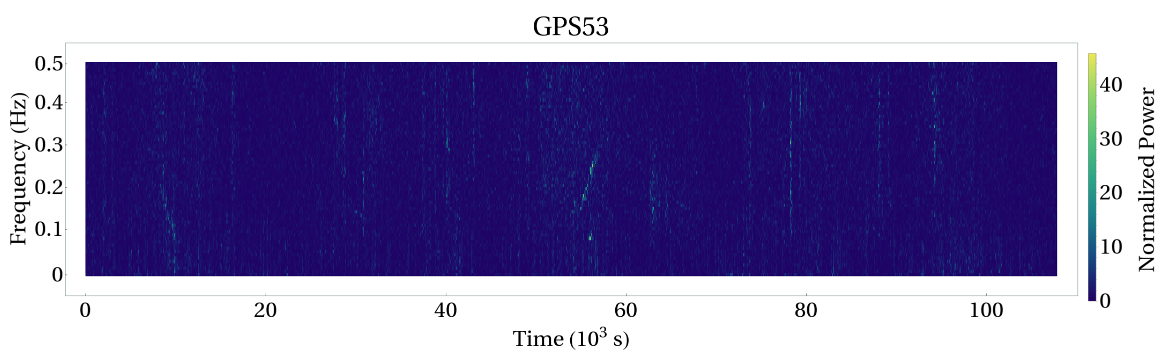
GPS53
Frequency (Hz)
Time (10^3 s)
Normalized Power
0 0.1 0.2 0.3 0.4 0.5
0 20 40 60 80 100
0 10 20 30 40

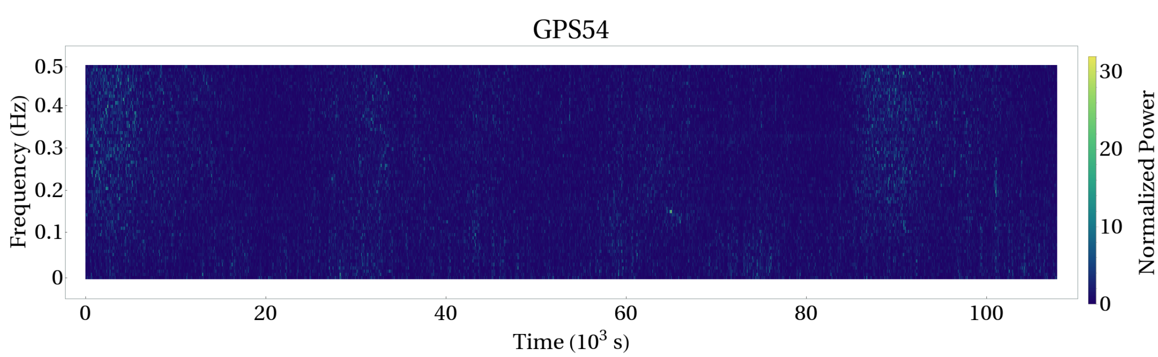
GPS54
Frequency (Hz)
Time (10^3 s)
Normalized Power
0 0.1 0.2 0.3 0.4 0.5
0 20 40 60 80 100
0 10 20 30

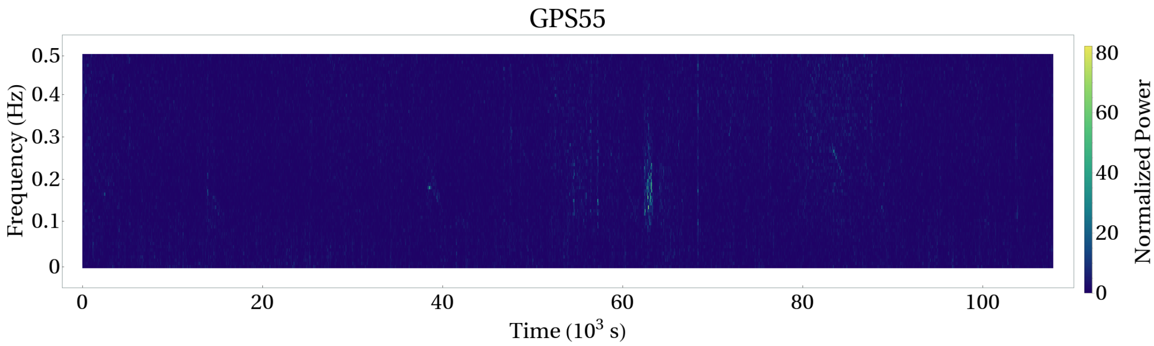
GPS55
Frequency (Hz)
Time (10^3 s)
Normalized Power

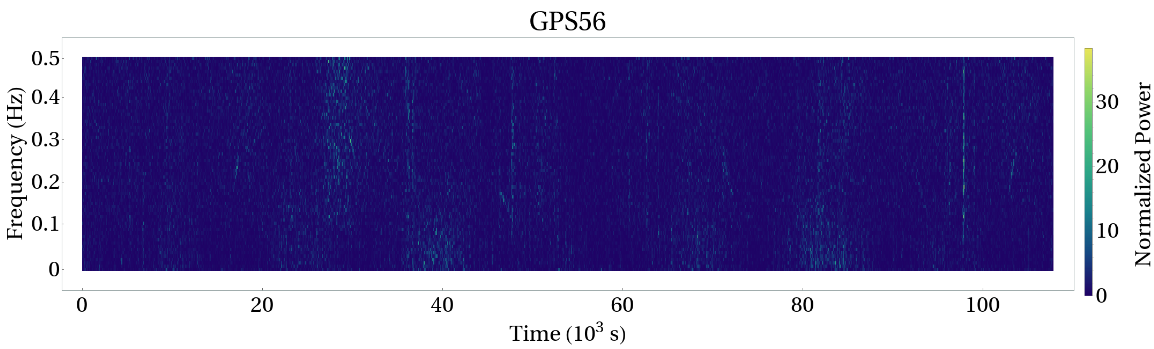
GPS56
Frequency (Hz)
Time (10^3 s)
Normalized Power

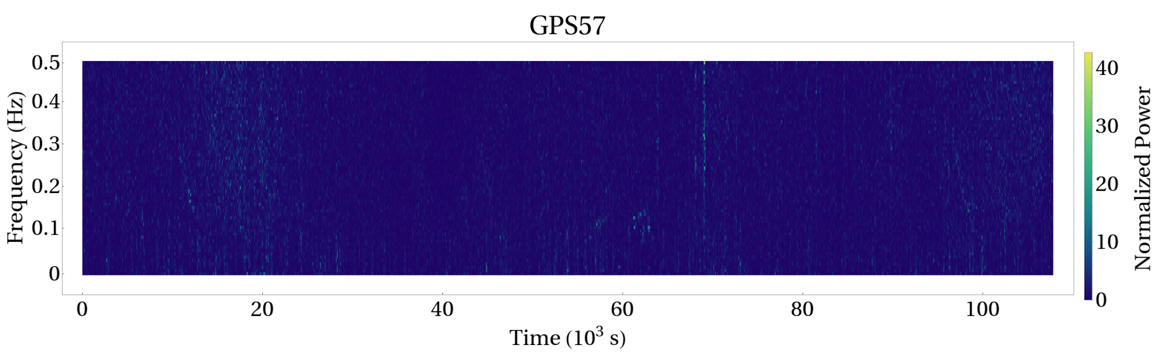
GPS57
Frequency (Hz)
Time (10^3 s)
Normalized Power

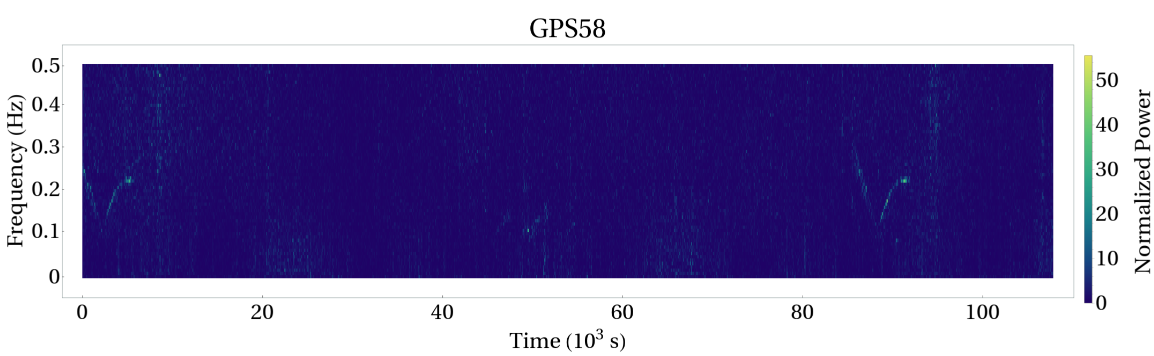
GPS58
Frequency (Hz)
Time (10^3 s)
Normalized Power

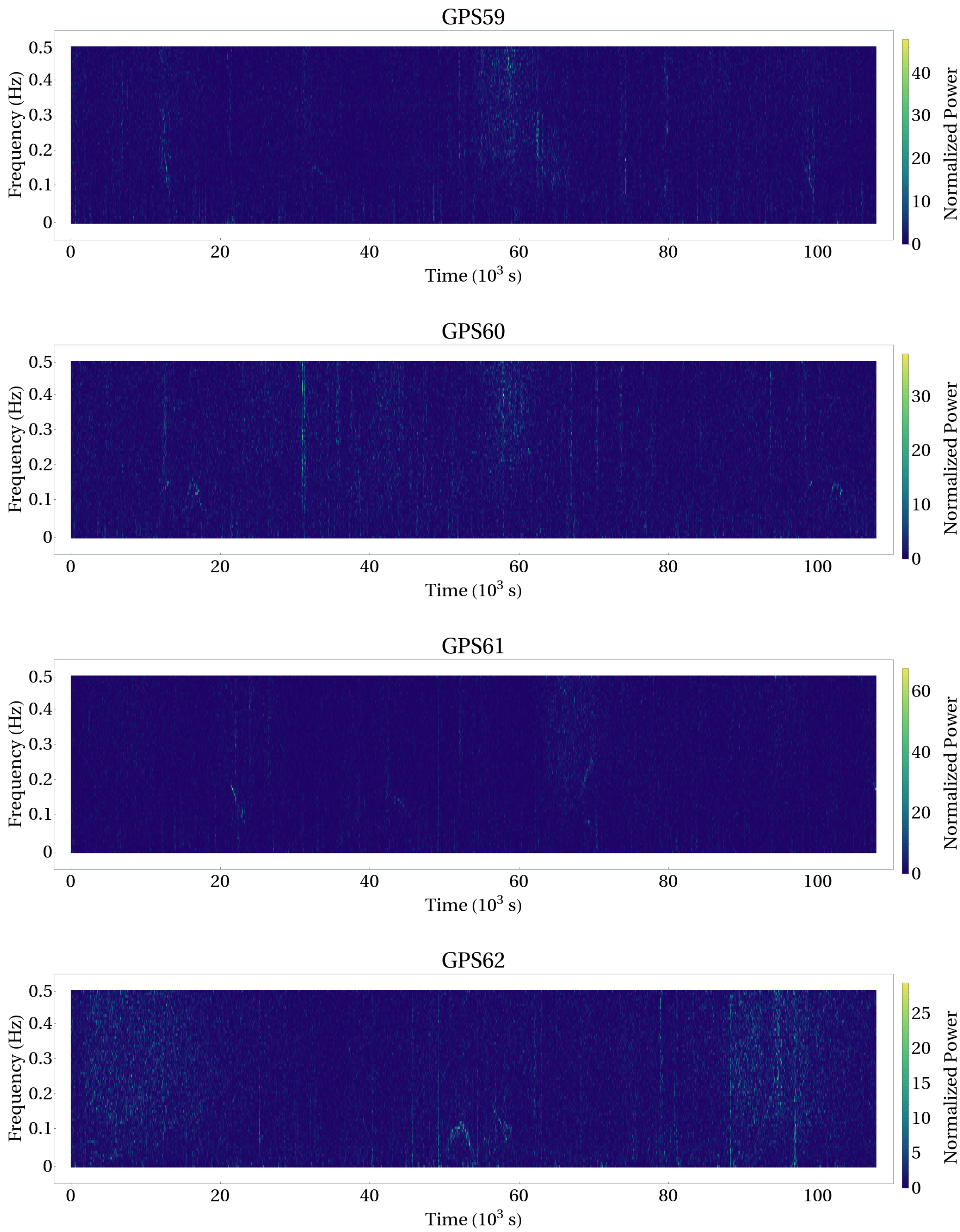
GPS59
GPS60
GPS61
GPS62
Frequency (Hz)
Time (10^3 s)
Normalized Power

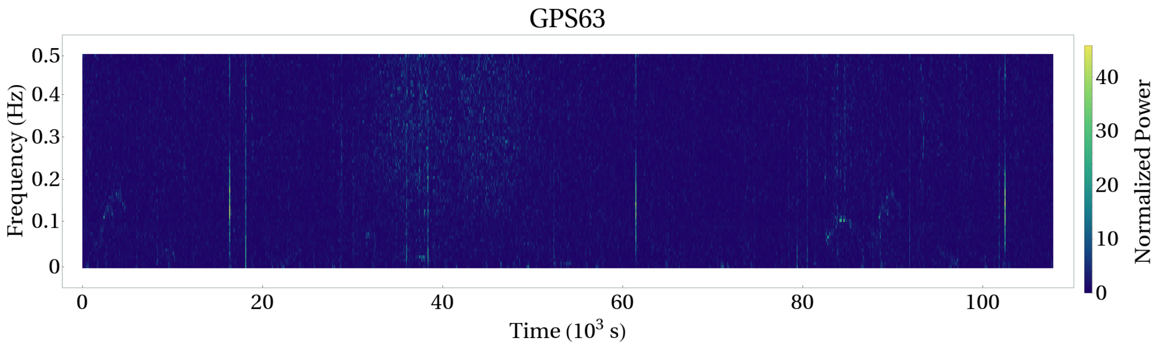
GPS63
Frequency (Hz)
0 0.1 0.2 0.3 0.4 0.5
0 20 40 60 80 100
Time (10^3 s)
Normalized Power
0 10 20 30 40

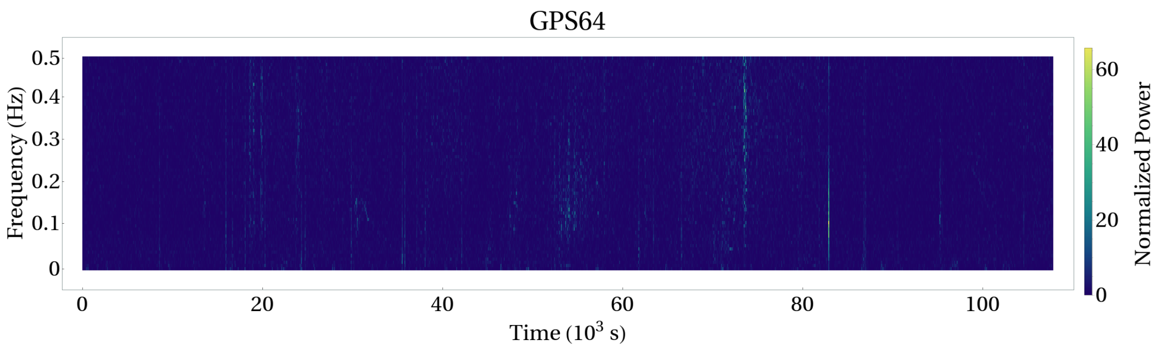
GPS64
Frequency (Hz)
0 0.1 0.2 0.3 0.4 0.5
0 20 40 60 80 100
Time (10^3 s)
Normalized Power
0 20 40 60

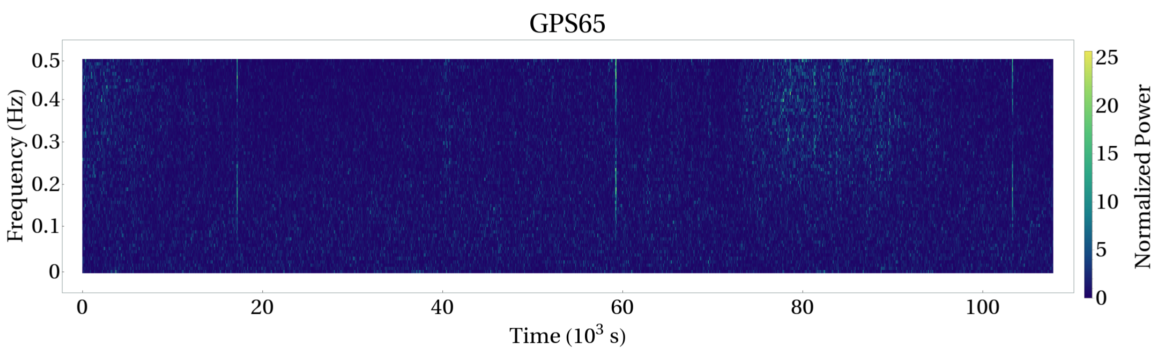
GPS65
Frequency (Hz)
0 0.1 0.2 0.3 0.4 0.5
0 20 40 60 80 100
Time (10^3 s)
Normalized Power
0 5 10 15 20 25

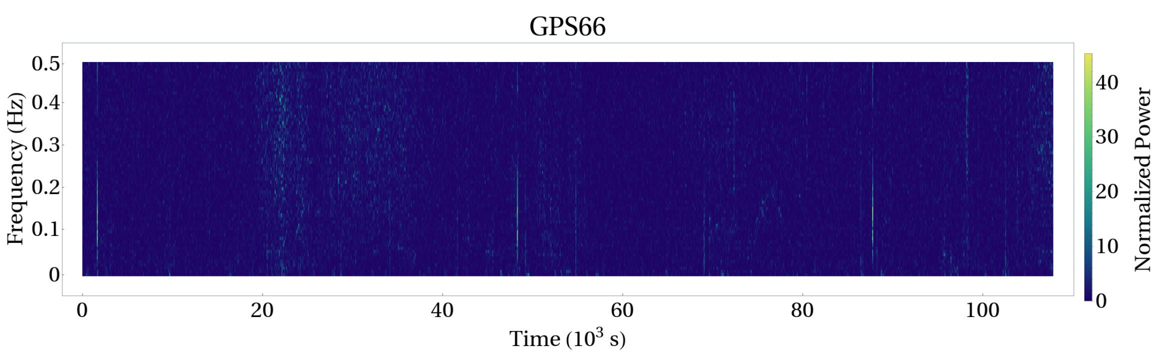
GPS66
Frequency (Hz)
0 0.1 0.2 0.3 0.4 0.5
0 20 40 60 80 100
Time (10^3 s)
Normalized Power
0 10 20 30 40

GPS67

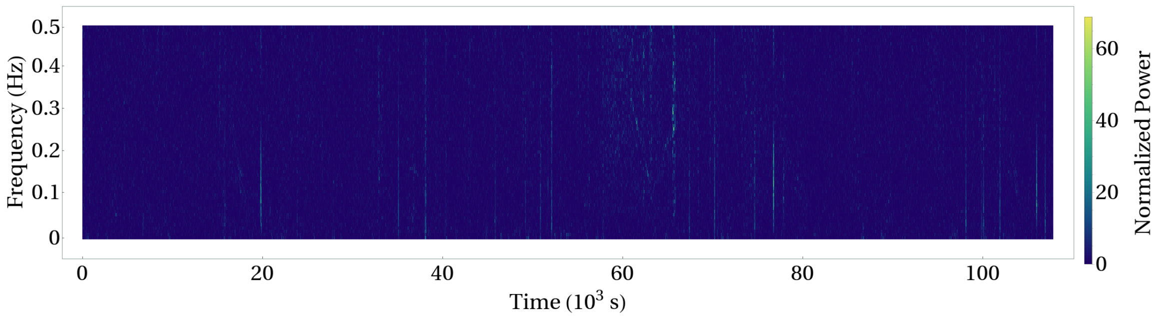

GPS68

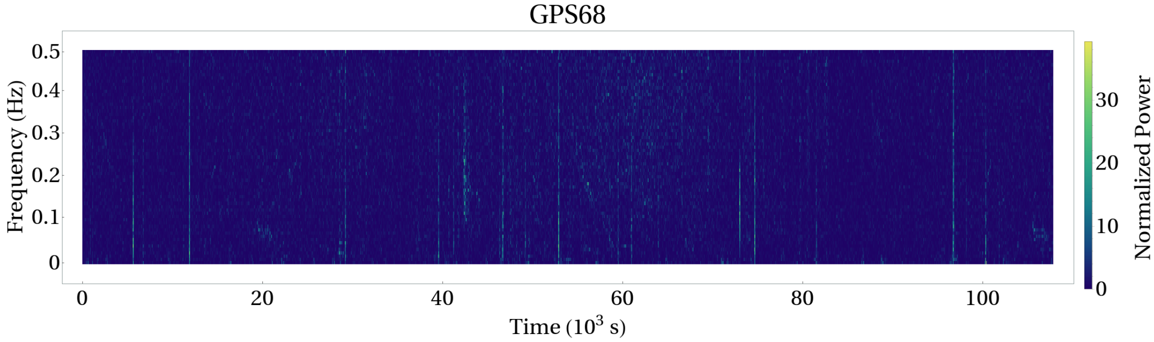

GPS69

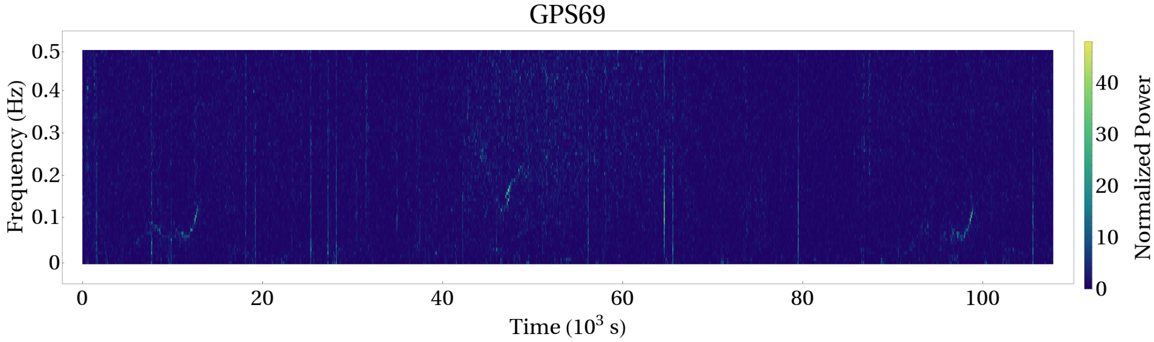

GPS70

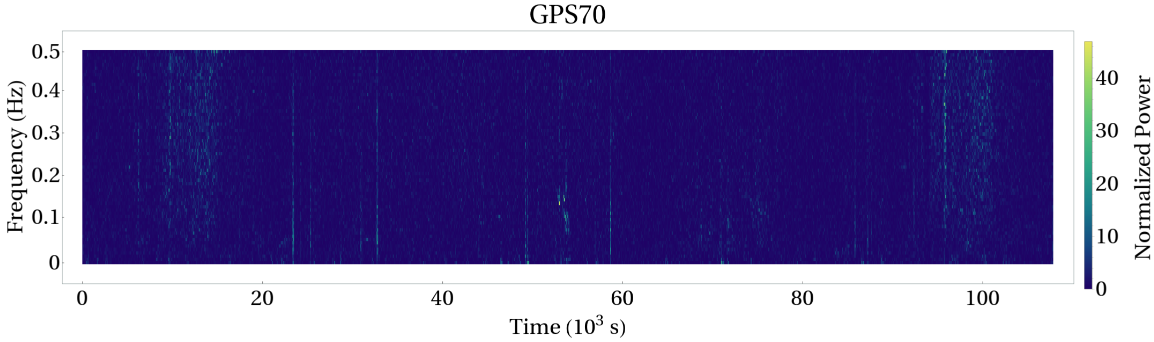

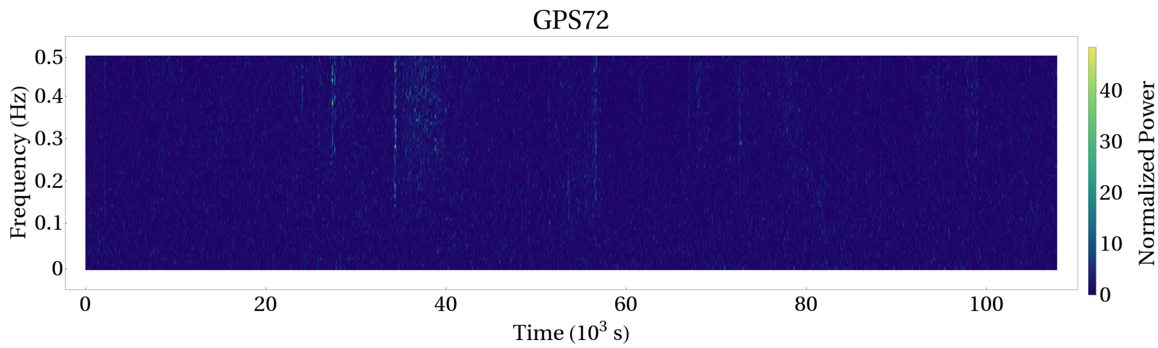
GPS72
Frequency (Hz)
0.5
0.4
0.3
0.2
0.1
0
0
20
40
60
80
100
Time (10^3 s)
Normalized Power
40
30
20
10
0

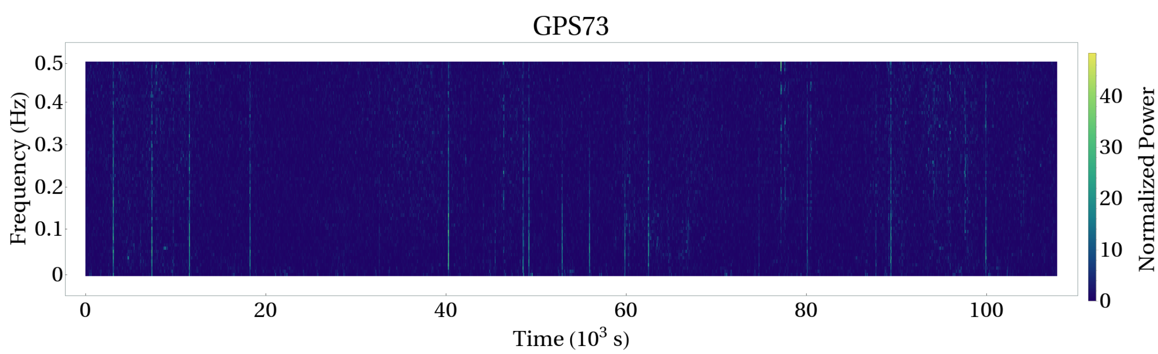
GPS73
Frequency (Hz)
0.5
0.4
0.3
0.2
0.1
0
0
20
40
60
80
100
Time (10^3 s)
Normalized Power
40
30
20
10
0

Bibliography

[1] Geoffrey Blewitt. *GPS and Space Based Geodetic Methods.* Vol. 3. Academic Press, Oxford, UK, 2007, pp. 351–390.

[2] "Evolution of the Global Navigation Satellite System (GNSS)". In: 96.12 (2008), pp. 1902–1917.

[3] Elliott D. Kaplan and Christopher J Hegarty. *Global Positioning System.* 3rd ed. Artech House, 2017, pp. 89–189.

[4] *GPS.gov: Space Segment.*

[5] Geoffrey Blewitt. "Carrier phase ambiguity resolution for the Global Positioning System applied to geodetic baselines up to 2000 km". In: *Journal of Geophysical Research: Solid Earth* 94.B8 (1989), pp. 10187–10203.

[6] Geoffrey Blewitt. "An Automatic Editing Algorithm for GPS data". In: *Geophysical Research Letters* 17.3 (1990), pp. 199–202.

[7] G. Petit and B. Luzum. "The 2010 Reference Edition of the IERS Conventions". In: *Reference Frames for Applications in Geosciences International Association of Geodesy Symposia* (2012), pp. 57–61.

[8] J. Kouba. "Improved relativistic transformations in GPS". In: *GPS Solutions* 8.3 (Sept. 2004), pp. 170–180.

[9] T. Rosenband et al. “Frequency Ratio of Al+ and Hg+ Single-Ion Optical Clocks; Metrology at the 17th Decimal Place”. In: *Science* 319.5871 (2008), pp. 1808–1812.

[10] BP Abbott et al. “Multi-messenger observations of a binary neutron star merger”. In: *Astrophysical Journal Letters* 848.2 (2017), p. L12.

[11] D Budker and A Derevianko. “A data archive for storing precision measurements”. In: *Physics Today* 68 (2015), p. 9.

[12] MS Safronova et al. “Search for new physics with atoms and molecules”. In: *Reviews of Modern Physics* 90.2 (2018), p. 025008.

[13] Andrei Derevianko and Maxim Pospelov. “Hunting for topological dark matter with atomic clocks”. In: *Nature Physics* 10.12 (2014), p. 933.

[14] P Wcisło et al. “New bounds on dark matter coupling from a global network of optical atomic clocks”. In: *Science Advances* 4.12 (2018), p. 4869.

[15] Benjamin P Abbott et al. “Observation of gravitational waves from a binary black hole merger”. In: *Physical review letters* 116.6 (2016), p. 061102.

[16] Benjamin P Abbott et al. “GW170814: a three-detector observation of gravitational waves from a binary black hole coalescence”. In: *Physical Review Letters* 119.14 (2017), p. 141101.

[17] Benjamin P Abbott et al. “GW170817: observation of gravitational waves from a binary neutron star inspiral”. In: *Physical Review Letters* 119.16 (2017), p. 161101.

[18] Benjamin M Roberts et al. “Search for domain wall dark matter with atomic clocks on board global positioning system satellites”. In: *Nature Communications* 8.1 (2017), p. 1195.

[19] BM Roberts et al. “Search for transient ultralight dark matter signatures with networks of precision measurement devices using a Bayesian statistics method”. In: *Physical Review D* 97.8 (2018), p. 083009.

[20] Andrei Derevianko. “Detecting dark-matter waves with a network of precision-measurement tools”. In: *Physical Review A* 97.4 (2018), p. 042506.

[21] J. Preskill, M. B. Wise, and F. Wilczek. “Cosmology of the invisible axion”. In: *Physics Letters B* 120 (1983), p. 127.

[22] L. F. Abbott and P. Sikivie. “A cosmological bound on the invisible axion”. In: *Physics Letters B* 120 (1983), p. 133.

[23] M. Dine and W. Fischler. “The not-so-harmless axion”. In: *Physics Letters B* 120 (1983), p. 137.

[24] Leanne D. Duffy and Karl van Bibber. “Axions as dark matter particles”. In: *New J. Phys.* 11 (2009), p. 105008.

[25] P. W. Graham et al. “Experimental Searches for the Axion and Axion-Like Particles”. In: *Annual Review of Nuclear and Particle Science* 65 (2015), p. 485.

[26] Nima Arkani-Hamed et al. “Ghost condensation and a consistent infrared modification of gravity”. In: *J. High Energy Phys.* 05 (2004), p. 074.

[27] V. Flambaum, S. Lambert, and M. Pospelov. “Scalar-tensor theories with pseudoscalar couplings”. In: *Phys. Rev. D* 80 (2009), p. 105021.

[28] A. Joyce et al. “Beyond the cosmological standard model”. In: *Physics Reports* 568 (2015), p. 1.

[29] Peter W. Graham, David E. Kaplan, and Surjeet Rajendran. “Cosmological Relaxation of the Electroweak Scale”. In: *Phys. Rev. Lett.* 115 (2015), p. 221801.

[30] R. Peccei and H. Quinn. “CP conservation in the presence of pseudoparticles”. In: *Phys. Rev. Lett.* 38 (1977), p. 1440.

[31] R. Peccei and H. Quinn. “Constraints imposed by CP conservation in the presence of pseudoparticles”. In: *Phys. Rev. D* 16 (1977), p. 1791.

[32] S. Weinberg. “A New Light Boson?” In: *Phys. Rev. Lett.* 40 (1978), p. 223.

[33] F. Wilczek. “Problem of Strong P and T Invariance in the Presence of Instantons”. In: *Phys. Rev. Lett.* 40 (1978), p. 279.

[34] M. Dine, W. Fischler, and M. Srednicki. “A simple solution to the strong CP problem with a harmless axion”. In: *Phys. Lett.* 104B (1981), p. 199.

[35] M. Shifman, A. Vainshtein, and V. Zakharov. “Can confinement ensure natural CP invariance of strong interactions?” In: *Nucl. Phys. B* 166 (1980), p. 493.

[36] J. Kim. “Weak-interaction singlet and strong CP invariance”. In: *Phys. Rev. Lett.* 43 (1979), p. 103.

[37] David Bailin and Alex Love. “Kaluza-Klein theories”. In: *Rep. Prog. Phys.* 50 (1987), p. 1087.

[38] P. Svrcek and E. Witten. “Axions in string theory”. In: *J. High Energy Phys.* 06 (2006), p. 051.

[39] A. Arvanitaki et al. “String axiverse”. In: *Phys. Rev. D* 81 (2010), p. 123530.

[40] Donato Bini, Andrea Geralico, and Antonello Ortolan. “Deviation and precession effects in the field of a weak gravitational wave”. In: *Physical Review D* 95.10 (2017), p. 104044.

[41] Daniel Baumann, Horng Sheng Chia, and Rafael A Porto. “Probing ultralight bosons with binary black holes”. In: *Phys. Rev. D* 99.4 (2019), p. 044001.

[42] G. Raffelt and D. Seckel. “Bounds on exotic-particle interactions from SN1987A”. In: *Phys. Rev. Lett.* 60 (1988), p. 1793.

[43] G. G. Raffelt. “Particle physics from stars”. In: *Annu. Rev. Nucl. Part. Sci.* 49 (1999), p. 163.

[44] A. Iwazaki. “Axion stars and fast radio bursts”. In: *Phys. Rev. D* 91 (2015), p. 023008.

[45] Igor I Tkachev. “Fast radio bursts and axion miniclusters”. In: *JETP Letters* 101 (2015), p. 1.

[46] Francis Halzen. “High-energy neutrino astrophysics”. In: *Nature Physics* 13.3 (2017), p. 232.

[47] Jamie Holder et al. “The first VERITAS telescope”. In: *Astroparticle Physics* 25.6 (2006), pp. 391–401.

[48] WB Atwood et al. “The large area telescope on the Fermi gamma-ray space telescope mission”. In: *The Astrophysical Journal* 697.2 (2009), p. 1071.

[49] R Agnese et al. “Improved WIMP-search reach of the CDMS II germanium data”. In: *Physical Review D* 92.7 (2015), p. 072003.

[50] E Aprile et al. “First dark matter search results from the XENON1T experiment”. In: *Physical Review Letters* 119.18 (2017), p. 181301.

[51] Asimina Arvanitaki and Sergei Dubovsky. “Exploring the string axiverse with precision black hole physics”. In: *Physical Review D* 83.4 (2011), p. 044026.

[52] Edward Hardy and Robert Lasenby. “Stellar cooling bounds on new light particles: plasma mixing effects”. In: *Journal of High Energy Physics* 2017.2 (2017), p. 33.

[53] E.N. Alexeyev et al. “Detection of the neutrino signal from SN 1987A in the LMC using the INR Baksan underground scintillation telescope”. In: *Physics Letters B* 205.2–3 (1988), pp. 209–214.

[54] L. Kepko et al. “Interhemispheric observations of impulsive nitrate enhancements associated with the four large ground-level solar cosmic ray events (1940-1950)”. In: *Journal of Atmospheric and Solar-Terrestrial Physics* 71.17-18 (2009), pp. 1840–1845.

[55] M. G. Aartsen et al. “Multimessenger observations of a flaring blazar coincident with high-energy neutrino IceCube-170922A”. In: *Science* 361.6398 (2018).

[56] Asimina Arvanitaki, Masha Baryakhtar, and Xinlu Huang. “Discovering the QCD axion with black holes and gravitational waves”. In: *Physical Review D* 91.8 (2015), p. 084011.

[57] Asimina Arvanitaki et al. “Black hole mergers and the QCD axion at Advanced LIGO”. In: *Physical Review D* 95.4 (2017), p. 043001.

[58] Masha Baryakhtar, Robert Lasenby, and Mae Teo. “Black hole superradiance signatures of ultralight vectors”. In: *Physical Review D* 96.3 (2017), p. 035019.

[59] Hirotaka Yoshino and Hideo Kodama. “Probing the string axiverse by gravitational waves from Cygnus X-1”. In: *Progress of Theoretical and Experimental Physics* 2015.6 (2015).

[60] Benjamin P Abbott et al. “GW170608: Observation of a 19 solar-mass binary black hole coalescence”. In: *The Astrophysical Journal Letters* 851.2 (2017), p. L35.

[61] John David Jackson. *Classical Electrodynamics, 3rd Edition.* 1998.

[62] Savas Dimopoulos Asimina Arvanitaki and Ken Van Tilburg. “Sound of Dark Matter: Searching for Light Scalars with Resonant-Mass Detectors”. In: *Physical Review Letters* 116.031102 (2016).

[63] N. Hinkley et al. “An Atomic Clock with 10^{-18} Instability”. In: *Science* 341.1 (2013), pp. 1215–1218.

[64] Y.Y. Jiang et al. "Making optical atomic clocks more stable with 10^{16}-level laser stabilization". In: *Nature Photonics* 5 (Jan. 2011), p. 158.

[65] V. V. Flambaum. "Enhanced Effect of Temporal Variation of the Fine Structure Constant and the Strong Interaction in ^{229}Th". In: *Physical Review Letters* 97.092502 (2006).

[66] GA Kazakov et al. "Performance of a ^{229}Thorium solid-state nuclear clock". In: *New Journal of physics* 14.8 (2012), p. 083019.

[67] Keith A. Olive and Maxim Pospelov. "Environmental dependence of masses and coupling constants". In: *Physical Review D* 77 (4 2008), p. 043524.

[68] Benjamin P Abbott et al. "The rate of binary black hole mergers inferred from advanced LIGO observations surrounding GW150914". In: *The Astrophysical journal letters* 833.1 (2016), p. L1.

[69] Yacine Ali-Haımoud, Ely D Kovetz, and Marc Kamionkowski. "Merger rate of primordial black-hole binaries". In: *Physical Review D* 96.12 (2017), p. 123523.

[70] Michela Mapelli and Nicola Giacobbo. "The cosmic merger rate of neutron stars and black holes". In: *Monthly Notices of the Royal Astronomical Society* 479.4 (2018), pp. 4391–4398.

[71] K Belczynski et al. "Binary neutron star formation and the origin of GW170817". In: *arXiv:1812.10065* (2018).

[72] Martyna Chruslinska et al. "Double neutron stars: merger rates revisited". In: *Monthly Notices of the Royal Astronomical Society* 474.3 (2017), pp. 2937–2958.

[73] Warren G. Anderson et al. "Excess power statistic for detection of burst sources of gravitational radiation". In: *Phys. Rev. D* 63 (4 Jan. 2001), p. 042003.

[74] Michele Maggiore. *Gravitational Waves: Volume 1: Theory and Experiments*. New York: Oxford University Press, 2008.